University of Thessaly
School of Engineering
Department of Mechanical Engineering

Diploma Thesis

An isotropic elastic-plastic model with hydrogen effects: Application to the problem of Mode-I fracture of a blunting crack

by

KONSTANTINOS NARIS

Submitted in Partial Fulfilment of the
Requirements for Diploma in Mechanical Engineering
2024

Approved by the Three Members of the Advisory Committee:

First Member (Supervisor)

Professor Nikolaos Aravas
Department of Mechanical Engineering, University of Thessaly

Second Member

Professor Gregory N. Haidemenopoulos
Department of Mechanical Engineering, University of Thessaly

Third Member

Associate Professor Michalis Agoras
Department of Mechanical Engineering, University of Thessaly

Abstract

An isotropic elastic-plastic model with hydrogen effects: Application to the problem of Mode-I fracture of a blunting crack

Naris Konstantinos

Supervisor: Professor N. Aravas

This work is concerned with the development of an isotropic constitutive model for metallic materials with hydrogen effects. The model takes into account the coupling between the mechanical and mass transfer phenomena and can be used for the numerical simulation of the well-known problem of hydrogen embrittlement. Computationally, two user subroutines have been developed in both ABAQUS/Standard and ABAQUS/Explicit (UMAT and VUMAT) while the model has been tested in the problem of Mode-I fracture under small-scale yielding hypothesis. Through the FEM simulations we investigate the effects of trapping on hydrogen transport using Oriani's equilibrium theory to relate the hydrogen in traps with the hydrogen in the lattice. Finally, we perform a comparative study between 2D and 3D simulations in ABAQUS/Explicit with appropriate boundary conditions.

Acknowledgements

This thesis was carried out in partial fulfilment of the requirements for the Diploma in Mechanical Engineering at the Department of Mechanical Engineering of University of Thessaly.

First and foremost I would like to express my sincere gratitude to my diploma thesis advisor, Professor Nikolaos Aravas for introducing me to solid mechanics, for instilling me with his knowledge, for the all the valuable advice and continuous guidance throughout my studies but more importantly for trusting me on this subject. His expertise and personality will always be a form of inspiration for me.

Secondly, I am deeply thankful to the members of the advisory committee Professor Gregory Haidemenopoulos and Associate Professor Michalis Agoras for all the valuable time they devoted in reviewing this thesis.

I would also like to thank Ph.D. candidate Socrates Xenos for his numerous insightful comments on this thesis, the abundant advice on the Abaqus Finite Element Software, and the LaTeX typesetting system.

I especially need to thank Aimlia for the undivided moral support, and for always being by my side. Without her, I would not be able to endure all the difficulties, nor achieve so much.

Finally and more importantly, I express my deepest gratitude to my parents Vasilis and Vasiliki and to my older sister Maria for all their love and support, without whom I would not be able to complete my studies.

Contents

List of Figures

List of Tables

Introduction

For a long time, hydrogen has been known to cause the degradation of the mechanical performance of metals, and this degradation is considered as a key technological challenge in many industrial applications. Hydrogen Embrittlement (HE) is a severe environmental type of failure and refers to mechanical damage of a metal due to the penetration of hydrogen into the metal causing loss in ductility and tensile strength. At specific temperatures hydrogen atoms can be absorbed into the metal lattice and diffuse through the grains. These hydrogen atoms may be present either as an atomic or combined molecular form. Regardless of the form hydrogen forms small bubbles at metal grain boundaries. Metals and alloys are degraded in the presence of hydrogen and the levels of loads these materials can afford are usually lower compared to those that hydrogen free materials can sustain.

From a mechanics point of view, extensive studies have been done to determine the mechanisms that are responsible for HE. One of them is the mechanism of Hydrogen-Enhanced Localized Plasticity (HELP). Observations showed that in a range of temperatures and strain rates, there is increased dislocation mobility due to hydrogen. Therefore, hydrogen reduces the applied stress necessary to move a dislocation through a field of obstacles which results in localized plasticity.

A particularly important aspect of HE is that there exists a transport stage of hydrogen to the sites where degradation occurs. To fully model this and other failure mechanisms we need to solve the hydrogen diffusion equations to determine how hydrogen is distributed inside the material and couple this with the mechanical constitutive response of the material. Diffusion equations are derived from Fick's law which describes hydrogen flux due to chemical potential.

In Chapter 1 the theory of the HE problem is introduced. The various types of HE and the mechanisms underlying hydrogen-induced mechanical failure as well as the hydrogen transport mechanisms and plasticity are discussed. The constitutive model is presented in Chapter 2 outlining the formulation of the problem for hydrogen diffusion and the elastic-plastic model. Also, the heat transfer analogy for an efficient implementation of the model in a finite element setting is briefly discussed. Finally, in Chapter 3, the results from the application of the model to the problem of the Mode-I fracture of a blunting crack tip under plane strain, small scale yielding conditions are presented.

Standard notation is used throughout. Boldface symbols denote tensors the orders of which are indicated by the context. All tensor components are written with respect to a fixed Cartesian coordinate system with base vectors $\mathbf{e}_i$ $(i = 1, 2, 3)$, and the summation

convention is used for repeated Latin indices, unless otherwise indicated. The prefice det indicates the determinant, a superscript T the transpose, a superposed dot the material time derivative, and the superscripts sym and $skew$, enclosed in parentheses, the symmetric and anti-symmetric parts of a second order tensor. Let $\mathbf{a}$, $\mathbf{b}$ be vectors, $\mathbf{A}$, $\mathbf{B}$ second-order tensors, and $\boldsymbol{\mathcal{C}}$, $\boldsymbol{\mathcal{D}}$ two fourth-order tensors; the following products are used in the text: $(\mathbf{a}\,\mathbf{b})_{ij} = a_i\, b_j$, $\mathbf{A} : \mathbf{B} = A_{ij}\, B_{ij}$, $(\mathbf{A}\cdot\mathbf{B})_{ij} = A_{ik}\, B_{kj}$, $(\mathbf{A}\,\mathbf{B})_{ijkl} = A_{ij}\, B_{kl}$, $(\boldsymbol{\mathcal{C}} : \mathbf{A})_{ij} = \mathcal{C}_{ijkl}\, A_{kl}$, and $(\boldsymbol{\mathcal{C}} : \boldsymbol{\mathcal{D}})_{ijkl} = \mathcal{C}_{ijpq}\, \mathcal{D}_{pqkl}$. The inverse $\boldsymbol{\mathcal{C}}^{-1}$ of a fourth-order tensor $\boldsymbol{\mathcal{C}}$ that has the "minor" symmetries $\mathcal{C}_{ijkl} = \mathcal{C}_{jikl} = \mathcal{C}_{ijlk}$ is defined so that $\boldsymbol{\mathcal{C}} : \boldsymbol{\mathcal{C}}^{-1} = \boldsymbol{\mathcal{C}}^{-1} : \boldsymbol{\mathcal{C}} = \boldsymbol{\mathcal{I}}$, where $\boldsymbol{\mathcal{I}}$ is the symmetric fourth-order identity tensor with Cartesian components $\mathcal{I}_{ijkl} = (\delta_{ik}\,\delta_{jl} + \delta_{il}\,\delta_{jk})/2$, δ_{ij} being the Kronecker delta.

Chapter 1

Theory

1.1 Explanation of the problem

1.1.1 Introduction to hydrogen embrittlement

Exprerimental investigations and fractography analysis conducted on iron and steels demonstrate an adverse impact of hydrogen on their mechanical properties. When hydrogen is absorbed into the material it can cause a decrease in ductility and load carrying ability. Metals and alloys are degraded in the presence of hydrogen and become brittle because of the introduction and diffusion of hydrogen into the material. Hydrogen can enter metals only in the form of atoms or hydrogen ions. Gaseous hydrogen, at ambient temperature, is not absorbed by metals because it is in molecular form and pairs of atoms are tightly bound together. However, as the temperature rises, the molecules tend to dissociate into individual atoms allowing absorption. In steels the diffusible hydrogen ions come from water introduced by a wet electrochemical process and is a completely different high temperature hydrogen attack process. This phenomenon is known as Hydrogen Embrittlement (HE) and the degree of embrittlement is influenced both by the amount of hydrogen absorbed and the micro-structure of the material.

1.1.2 Different types of hydrogen embrittlement

In order to categorize HE, the embrittled systems can be divided into non-hydride formers and in hydride formers. More specifically there are three different types of HE mentioned in the literature; hydrogen reaction embrittlement (HRE), internal hydrogen embrittlement (IHE), and hydrogen environment embrittlement (HEE) [2].

For the first type (HRE), brittle phases and/or vapor are formed when hydrogen reacts with metals and alloying elements. In titanium, HRE occurs due to formation of hydrides. On the contrary, hydrogen does not form hydrides in steel. HRE is an irreversible “process”, and the mechanical properties of the material can’t be restored through heat treatment. The second type (IHE) occurs when the material undergoes prolonged periods of elevated

temperature and high hydrogen pressure, or during activities like welding, melting or chemical reactions. The hydrogen concentration influences the magnitude of the embrittlement, and the cracks initiate inside the material. Using an appropriate heat treatment cycle, the embrittlement can be completely prevented. Lastly, HEE arises when solid metals absorb hydrogen. Elevating hydrogen pressure leads to increased HEE occurrence. HEE is usually most severe at room temperature, mainly because both hydrogen transportation mechanisms (dislocations and diffusions) are active. The impact of strain rate on HEE can also be notable, with higher rates diminishing its effect. This outcome is attributed to augmented dislocation movement and reduced hydrogen transfer into the material.

1.2 Mechanisms

Despite decades of intensive studies, the micro-scale mechanisms of the hydrogen induced mechanical failure of materials remain a subject of debate [3]. Several hypotheses have been proposed and thoroughly examined. For non-hydride forming materials, two are the most viable of the many hypotheses that have been proposed and tested. These are the Hydrogen Enhanced-Decohesion mechanism (HEDE) and the Hydrogen-Enhanced Localized Plasticity mechanism (HELP)

1.2.1 Hydrogen-Enhanced Decohesion mechanism (HEDE)

One of the earliest methods for demonstrating how atomic hydrogen alters the characteristics of materials is the HEDE mechanism. It was introduced first by Troiano [4] and improved by Oriani [5]. According to the HEDE theory, metal atoms' bonds will weaken as a result of hydrogen atoms accumulating in areas with high triaxial stress. More specifically, this method is based on the hypothesis that the solute hydrogen reduces the cohesive force and, consequently, the energy needed to generate the cleavage surface, which are needed to separate the crystal along a crystallographic plane, giving rise to a reduced fracture toughness [6], [7]. In addition, hydrogen atoms will cause the bonds of metal atoms to deteriorate leading to premature brittle material fracture along grain boundaries. This hydrogen concentration-dependent HE mechanism is also known as a Hydrogen-Induced Decohesion (HID) [8]. The hypothesis applies to brittle fracture but does not explain fracture followed by plasticity.

1.2.2 Hydrogen-Enhanced Localized Plasticity mechanism (HELP)

Beachem [9] was the first to suggest that in the HE problem the failure occurs by locally ductile processes. The HELP mechanism implies that hydrogen enhances the dislocation mobility by reducing the elastic interaction energy between dislocations. As a result, the presence of hydrogen diminishes the required stress for displacing a dislocation through a field of obstacles, leading to a phenomenon that encourages the softening of the material [6]. Even while hydrogen increases plasticity at a very localized (microscopic) level, the

material nevertheless exhibits brittle behavior on a larger scale (reduced strain to failure, lower fracture strength).

1.3 Hydrogen transport and plasticity

A particularly important aspect of hydrogen embrittlement is that there exists a transport stage of hydrogen to the sites where degradation occurs. Hydrogen transport through the materials is typically attributed to diffusion occurring within the normal interstitial lattice sites (NILS). Transported hydrogen resides either at NILS or at trapping sites, like grain boundaries. First, Johnson and Troiano [10] concluded that the HE phenomenon is controlled by the diffusion of hydrogen into the crack tip region and is strongly influenced by hydrostatic stress gradients. The amount of hydrogen that has been solved in a metal is influenced by hydrogen transport and hydrogen solubility. The solution's hydrogen content is also influenced by variables including the hydrogen pressure, temperature, microstructure, and chemistry of the material [2]. Therefore, the analysis of the hydrogen transport processes should precede any attempt to address the issue of hydrogen embrittlement related failures.

1.3.1 Hydrogen lattice solubility

The NILS concentration can be expressed based on the interstice type and the lattice structure of the host metal as follows:

$$C_L = \theta_L \beta N_L \tag{1.1}$$

where C_L is the number of hydrogen atoms per unit lattice volume, θ_L denotes the occupancy of the available sites and is dimensionless, β denotes the number of NILS per solvent atom and N_L denotes the number of solvent lattice atoms per unit lattice volume. It is important to mention that in a given material, lattice parameters β and N_L are fixed. Also, given that V_M is the molar volume of the host lattice expressed in units of volume per lattice mole, N_L can be calculates as:

$$N_L = \frac{N_A}{V_M} \tag{1.2}$$

where $N_A = 6.0232 \times 10^{23}$ atoms per moles is Avogadro's number.

1.3.2 Trapping

The hydrogen can become trapped inside the material by adhering to impurities, structural flaws, or micro-structural components like carbides in alloys. Any metallurgical defect inside the material can act as a trap for hydrogen. These traps can be divided according to their energy into reversible and irreversible. When the required energy for hydrogen release is low, hydrogen can easily leave the traps (reversible traps) while if higher energy is required, hydrogen release is more difficult to occur (irreversible traps). The material traps

will prevent the diffusion of hydrogen. The concentration of hydrogen at trapping sites can be expressed as follows:

$$C_T = \theta_T \alpha N_T \tag{1.3}$$

where C_T is the number of trapped hydrogen atoms per unit lattice volume, α denotes the number of hydrogen atoms sites per trap, θ_T denotes the occupancy of the available sites (is the ratio of occupied sites to the total available) and N_T denotes the number of traps per unit lattice volume. The amount of hydrogen trapped in the reversible traps is always in equilibrium with the lattice hydrogen, according to Oriani's theory [5].

$$\frac{\theta_T}{1-\theta_T} = \frac{\theta_L}{1-\theta_L} K \tag{1.4}$$

where K is given by:

$$K = e^{-\frac{\Delta \bar{H}_B}{RT}} \tag{1.5}$$

where K is dimensionless of order 10^{10}, $\Delta \bar{H}_B$ is the trap binding energy, inherently negative, R is the gas constant and T is the absolute temperature. For $\theta_L \ll 1$ and by using equations (1.2), (1.3) and (1.4) :

$$C_T = \frac{K \frac{\alpha N_T}{\beta N_L} C_L}{1 + \frac{K}{\beta N_L} C_L} \tag{1.6}$$

which characterizes the equilibrium relationship between C_L and C_T in terms of material parameters.

1.3.3 Hydrogen lattice diffusion

Chemical potential gradients serve as the driving force for this diffusion process. At low concentrations where there is minimal interaction between the diffusing species, and the diffusion rate depends solely on hydrogen mobility, one can establish a relationship between the hydrogen flux ($\mathbf{J}$) and the gradient of the chemical potential (μ) as follows:

$$\mathbf{J} = \frac{D C_L}{RT} \nabla \mu \tag{1.7}$$

where D is the lattice diffusion constant that is assumed to be independent of stress but is dependent on temperature.This is because when temperature increases, the kinetic energy of the particles increases. The increased motion of the particles causes them to diffuse faster. Therefore, at higher temperatures, the rate at hydrogen will diffuse faster than at lower temperatures. The diffusion coefficient increases exponentially according to equation:

$$D = D_0 \times e^{\frac{-Q}{RT}} \tag{1.8}$$

where T is the temperature, Q is the activation energy, D_0 is the diffusion constant, and R is the gas constant [11]. Generally, when a system is subjected to external stress and operates

under the conditions where equation (1.7) holds true, its behaviour can be expressed while the pressure and temperature remain constant:

$$\mu = \mu^0 + RT \ln \frac{C_L}{C_L^0} + \mu_\sigma \tag{1.9}$$

where μ^0 is the chemical potential in the standard state, C_L^0 is the concentration in the absence of stress and μ_σ is the stress dependent part of μ. Substituting (1.9) into (1.7), the hydrogen flux can be expressed as follows:

$$\mathbf{J} = -D\nabla C_L - \frac{DC_L}{RT}\nabla \mu_\sigma \tag{1.10}$$

Assuming that NILS hydrogen causes only dilitational distortion to the lattice, one can write:

$$\mu_\sigma = -\frac{\sigma_{kk}}{3} V_H = -pV_H \tag{1.11}$$

where p is the hydrostatic stress, V_H is the partial molar volume of hydrogen in solid solution and the repeated index summation convention is used. The assumption of dilitational distortion has been established as being accurate within a first-order approximation, as documented by Hirth [12]. Substitution of equation (1.11) into (1.10) then yields:

$$\mathbf{J} = -D\nabla C_L + \frac{DV_H}{RT} C_L \nabla p \tag{1.12}$$

Expression (1.12) shows that the hydrogen flux $\mathbf{J}$ at every point in the material depends not only the lattice concentration and its corresponding spatial gradient but it is also coupled to the stress state in the material through dependence on the pressure gradient ∇p. When there are steady state equilibrium conditions, ($\frac{\partial}{\partial t} = 0$) and the fields are homogeneous in an infinite body, the process takes place very slowly. The hydrogen concentration does change but is always at equilibrium and there is not hydrogen flux ($\mathbf{J} = 0$). Any required hydrogen is provided by an available reservoir. In this situation the steady state lattice concentration can be calculated as:

$$\begin{aligned}
\mathbf{J} = \mathbf{0} \Rightarrow \frac{1}{C_L(\mathbf{x})}\nabla C_L(\mathbf{x}) &= \frac{V_H}{RT}\nabla p(\mathbf{x}) \Rightarrow \frac{1}{C_L(\mathbf{x})}\frac{\partial C_L(\mathbf{x})}{\partial x_i} = \frac{V_H}{RT}\frac{\partial p(\mathbf{x})}{\partial x_i} \\
\Rightarrow \frac{\partial[\ln C_L(\mathbf{x})]}{\partial x_i} &= \frac{V_H}{RT}\frac{\partial p(\mathbf{x})}{\partial x_i} \Rightarrow \frac{\partial}{\partial x_i}\left[\ln C_L(\mathbf{x}) - \frac{V_H}{RT}p(\mathbf{x})\right] = 0 \\
\Rightarrow \left[\ln C_L(\mathbf{x}) - \frac{V_H}{RT}p(\mathbf{x})\right] &- \left[\ln C_L(\mathbf{x}^0) - \frac{V_H}{RT}p(\mathbf{x}^0)\right] = 0 \\
\Rightarrow ln\frac{C_L(\mathbf{x})}{C_L(\mathbf{x}^0)} &= \frac{V_H}{RT}\left[p(\mathbf{x}) - p(\mathbf{x}^0)\right] \\
\Rightarrow \boxed{C_L(\mathbf{x}) = C_L(\mathbf{x}^0)\exp\left\{\frac{V_H}{RT}\left[p(\mathbf{x}) - p(\mathbf{x}^0)\right]\right\}} &
\end{aligned} \tag{1.13}$$

1.3.4 Transport of hydrogen by moving dislocations

According to the plasticity model for HE, hydrogen increases the mobility of dislocations. Moving dislocations at the same moment may move hydrogen. Thus, in order to comprehend how hydrogen affects the material's mechanical properties, it is crucial to understand the transport of hydrogen through dislocations.

Under plastic deformation there are more dislocations which offer more space for hydrogen in the material. Additionally, the mobility of dislocations imposed by plastic deformation facilitates the transfer of hydrogen [13]. Bastien and Azou [14] suggested that moving dislocations could carry hydrogen and that a local high hydrogen concentration can develop when dislocations annihilate or intersect a void. Franck [15] observed that deformation enhances hydrogen outgassing of mild steel. Generally, hydrogen transport via dislocation results in the specimen saturating with hydrogen more rapidly compared to diffusion alone. Additionally, dislocations can convey hydrogen from the surface at high concentrations. There are two types of this transport behavior.

The first is when prior to plastic deformation, the material is completely infused with hydrogen. The hydrogen is initially evenly distributed, and the overall hydrogen content is constant. Under mechanical load, the hydrogen is redistributed from the lattice and old traps to the newly generated dislocations, while the dislocation motion starts. The moving dislocations carry or release the trapped hydrogen depending on their velocity. All the hydrogen will be left behind as it is spread across the lattice and possibly partially absorbed by static traps if the velocity is high enough. On the other hand moving dislocations transport the hydrogen at speeds close to or below a critical value. If the dislocation slows down, its hydrogen concentration can rise once more to a level above that of dislocations that move quickly. Therefore, dislocations that are halted or slowed down are hydrogen sinks.

The second case involves simultaneous hydrogen charge and plastic deformation. It is reasonable to expect that the dislocations traveling from the surface will transport hydrogen with a concentration corresponding to the external charging medium [7].

Chapter 2

Consitutive Model

In this chapter the constitutive model is presented. More specifically, the coupled governing equations of the initial-boundary value problem of hydrogen diffusion and the elastic-plastic boundary value problem are discussed. An algorithm for the integration of the constitutive equations is also analysed. Also an efficient method for the implementation of the constitutive model in a finite element setting is discussed.

2.1 The isotropic elastic-plastic model with hydrogen effects

2.1.1 Mass balance for hydrogen diffusion

Within this section, we move forward with the formulation of the mass balance for hydrogen diffusion. Considering an arbitrary volume V of material bounded by a surface S at a given temperature T and subject to external loading, hydrogen can be found within volume V, either within the NILS (C_L) or in trapping sites (C_T). As described by (1.6) these two populations are assumed to be in equilibrium. Any alteration in hydrogen concentrations C_L and C_T within V is accompanied by the flow of hydrogen through the surface S. Because the mass conservation requires that the rate of change of total hydrogen $(C_L + C_T)$ inside V be equal to the flux through S, the continuity equation takes the following form:

$$\frac{d}{dt}\int_V (C_L + C_T)\, dV + \int_S \mathbf{J}\cdot\mathbf{n}\, dS = 0 \tag{2.1}$$

where $\mathbf{n}$ is the outward unit surface normal vector and so $(-\mathbf{J}\cdot\mathbf{n})$ is the hydrogen enering V. Using the divergence theorem and by means of the arbitrariness of volume V, we arrive at the following partial differential equation for the hydrogen concentration:

$$\frac{d}{dt}(C_L + C_T) + \nabla\cdot\mathbf{J} = 0 \tag{2.2}$$

Using equations (1.3) and (1.12) one has:

$$\mathbf{J} = -D\nabla C_L + \frac{DV_H}{RT} C_L \nabla p \quad \Rightarrow \quad \nabla \cdot \mathbf{J} = -D\nabla^2 C_L + \frac{DV_H}{RT}\left(\frac{\partial C_L}{\partial x_i}\frac{\partial p}{\partial x_i} + C_L \nabla^2 p\right), \tag{2.3}$$

$$C_T = \theta_T \alpha N_T \quad \Rightarrow \quad \dot{C}_T = \alpha\left(\frac{\partial \theta_T}{\partial C_L}\dot{C}_L N_T + \theta_T \frac{\partial N_T}{\partial \bar{\varepsilon}^p}\dot{\bar{\varepsilon}}^p\right), \tag{2.4}$$

Substituting equations (2.3), (2.4) into equation (2.2) the diffusion equation becomes:

$$\boxed{\left(1 + \alpha\frac{\partial \theta_T}{\partial C_L} N_T\right)\dot{C}_L + \alpha\theta_T \frac{\partial N_T}{\partial \bar{\varepsilon}^p}\dot{\bar{\varepsilon}}^p - D\nabla^2 C_L + \frac{DV_H}{RT}\left(\frac{\partial C_L}{\partial x_i}\frac{\partial p}{\partial x_i} + C_L\nabla^2 p\right) = 0} \tag{2.5}$$

2.1.2 The elastic-plastic model with hydrogen effects

In the following, we describe the main ingredients of the proposed analytical model. The constitutive relationship for elastic-plastic behaviour is expressed using the rate-of-deformation tensor, denoted as $\mathbf{D}$, and the Jaumann stress rate of the Cauchy stress, represented as $\overset{\nabla}{\boldsymbol{\sigma}}$. The Jaumann stress rate is employed to fulfill the conditions of objectivity, ensuring material invariance under rigid body rotations, and it is defined as follows:

$$\overset{\nabla}{\boldsymbol{\sigma}} = \dot{\boldsymbol{\sigma}} + \boldsymbol{\sigma}\cdot\mathbf{W} - \mathbf{W}\cdot\boldsymbol{\sigma} \tag{2.6}$$

where $\dot{\boldsymbol{\sigma}}$ is the material time derivative of the Cauchy stress, and $\mathbf{D}$ and $\mathbf{W}$ are the rate-of-deformation and spin tensors that are equal to symmetric and antisymmetric parts of the velocity gradient $\mathbf{L}$, respectively. Since in the case of metallic materials the elastic strains are small, it is assumed that the total rate-of-deformation tensor is taken to be the sum of the elastic part $\mathbf{D}^e$, plastic part $\mathbf{D}^p$ and a part due to presence of hydrogen $\mathbf{D}^h$, i.e., (see [17])

$$\mathbf{D} = \mathbf{D^e} + \mathbf{D^p} + \mathbf{D^h} \tag{2.7}$$

The constitutive equations for the elastic and plastic behavior are treated separately and are later combined in order to yield the total effective elastic-plastic response of the material through equation 2.7.

2.1.3 Elasticity

The overall elastic behavior of the porous material is characterized using a hypoelastic constitutive equation of the form:

$$\mathbf{D}^e = \boldsymbol{\mathcal{M}}^e : \overset{\nabla}{\boldsymbol{\sigma}}, \quad \boldsymbol{\mathcal{M}}^e = \frac{1}{2\mu}\boldsymbol{\mathcal{K}} + \frac{1}{3\kappa}\boldsymbol{\mathcal{J}}, \quad \boldsymbol{\mathcal{J}} = \frac{1}{3}\boldsymbol{\delta}\boldsymbol{\delta}, \quad \boldsymbol{\mathcal{K}} = \boldsymbol{\mathcal{I}} - \boldsymbol{\mathcal{J}} \tag{2.8}$$

where, $\overset{\nabla}{\boldsymbol{\sigma}}$ is the co-rotational Jaumann derivative of the Cauchy stress $\boldsymbol{\sigma}$, $\boldsymbol{\mathcal{I}}$ is the symmetric fourth-order identity tensor, $(\boldsymbol{\mathcal{K}}, \boldsymbol{\mathcal{J}})$ are the deviatoric and hydrostatic fourth-order identity tensors and δ is the second-order identity tensor (Kronecker delta). Also, $\boldsymbol{\mathcal{M}}^e = (\boldsymbol{\mathcal{L}}^e)^{-1}$ is the fourth-order isotropic elastic compliance tensor, and (κ, μ) are the elastic bulk and shear moduli of the material.

2.1.4 Plasticity

The plastic part of the rate-of-deformation tensor is given by the usual "normality" rule:

$$\mathbf{D}^p = \dot{\bar{\varepsilon}}^p \mathbf{N}, \quad \mathbf{N} = \frac{3}{2\sigma_e}\boldsymbol{s}, \quad \mathbf{s} = \boldsymbol{\sigma} - p\boldsymbol{\delta}, \quad p = \frac{\sigma_{kk}}{3},\ \sigma_e = \sqrt{\frac{3}{2}\mathbf{s} : \mathbf{s}} \tag{2.9}$$

where σ_e is the equivalent von Mises stress. The yield condition is defined as:

$$\Phi(s, \bar{\varepsilon}^p, C_L) = \sigma_e(s) - \sigma_y(\bar{\varepsilon}^p, C_L) = 0 \tag{2.10}$$

where $\sigma_y(\bar{\varepsilon}^p, C_L)$ is the flow stress of the material given as:

$$\sigma_y(\bar{\varepsilon}^p, C_L) = f(c)\sigma_0\Big(1 + \frac{\bar{\varepsilon}^p}{\varepsilon_0}\Big) \quad f(c) = 1 - (1-\xi)c, \quad c = c\Big(C_L, \bar{\varepsilon}^p\Big) \tag{2.11}$$

$$c(C_L, \bar{\varepsilon}^p) = \frac{C_L + C_T\Big(C_L, \bar{\varepsilon}^p\Big)}{N_L}, \quad C_T\Big(C_L, \bar{\varepsilon}^p\Big) = \alpha\theta_T\Big(C_L\Big)N_T\Big(\bar{\varepsilon}^p\Big) \tag{2.12}$$

$$\theta_T\Big(C_L\Big) = \frac{K_T\theta_L\Big(C_L\Big)}{1 + K_T\theta_L\Big(C_L\Big) - \theta_L\Big(C_L\Big)}, \quad \theta\Big(C_L\Big) = \frac{C_L}{\beta N_L} \tag{2.13}$$

In the present work "one-way coupling" is considered (i.e., we do not consider the effect of hydrogen concentration on the flow stress of the material) so that $\xi = 1$. During plastic flow, the elastic constitutive equation becomes:

$$\overset{\nabla}{\boldsymbol{\sigma}} = \boldsymbol{\mathcal{L}}^e : \mathbf{D}^e = \boldsymbol{\mathcal{L}}^e : \Big(\mathbf{D} - \mathbf{D}^p - \mathbf{D}^h\Big) \tag{2.14}$$

Lastly, the part due to presence of hydrogen $\mathbf{D}^h$ of the total rate-of-deformation tensor $\mathbf{D}$ is calculated from the following expression:

$$\mathbf{D}^h = \frac{1}{3}\,\frac{\lambda\dot{c}}{1 + \frac{\lambda}{3}(c - c_0)}\boldsymbol{\delta} = \frac{1}{3}\underbrace{\Lambda(c)\dot{c}}_{\dot{\varepsilon}^h_\nu}\boldsymbol{\delta}, \quad \Lambda(c) = \frac{\lambda}{1 + \frac{\lambda}{3}(c - c_0)}, \quad c = c(C_L, \bar{\varepsilon}^p) \tag{2.15}$$

2.2 Numerical integration of the constitutive equations

In this section the equations for the integration of the constitutive model are presented. The main unknown is $\Delta\bar{\varepsilon}^p$. With $\Delta\bar{\varepsilon}^p$ known the deviatoric stress $\mathbf{s}_{n+1}$ at the end of the

increment can then be calculated. The procedure is as follows. Normality rule $(2.9)_1$ is integrated using a backward Euler scheme:

$$\Delta\boldsymbol{\varepsilon}^p = \Delta\bar{\varepsilon}^p \mathbf{N}_{n+1} \tag{2.16}$$

Also,

$$p_{n+1} = \kappa\varepsilon^e_{kk}\Big|_{n+1} = \kappa\Big(\varepsilon_{kk}\Big|_{n+1} - \varepsilon^h_{kk}\Big|_{n+1}\Big) \tag{2.17}$$

or

$$p_{n+1} = p_n + \kappa\Delta\varepsilon^e_{kk} = p_n + \kappa(\Delta\varepsilon_{kk} - \Delta\varepsilon^h_{kk}) = \underbrace{p_n + \kappa\Delta\varepsilon_{kk}}_{p^e} - \kappa\Delta\varepsilon^h_{kk} = p^e - \kappa\Delta\varepsilon^h_{kk} \tag{2.18}$$

with:

$$\varepsilon^h_{kk} = 3\ln\left[1 + \frac{\lambda}{3}\Big(c - c_0\Big)\right], \quad \Delta\varepsilon^h_{kk} = \frac{\lambda\Delta c}{1 + \frac{\lambda}{3}(c_{n+1} - c_0)} \tag{2.19}$$

the deviatoric stress $\mathbf{s}_{n+1}$ is integrated as follows:

$$\begin{aligned}
&\mathbf{s}_{n+1} = \mathbf{s}_n + 2G\Delta\mathbf{e}^e = \mathbf{s}_n + 2G(\Delta\mathbf{e} - \Delta\boldsymbol{\varepsilon}^p) = \underbrace{\mathbf{s}_n + 2G\Delta\mathbf{e}}_{s^e} - 2G\Delta\boldsymbol{\varepsilon}^p = \mathbf{s}^e - 2G\Delta\bar{\boldsymbol{\varepsilon}}^p\mathbf{N}_{n+1} \Rightarrow \\
&\mathbf{s}_{n+1} = s^e - 2G\Delta\bar{\varepsilon}^p\Big(\frac{3}{2\sigma_e|_{n+1}}\mathbf{s}_{n+1}\Big) \Rightarrow \\
&\mathbf{s}_{n+1} = \frac{1}{1 + \frac{3G\Delta\bar{\varepsilon}^p}{\sigma_e|_{n+1}}}\mathbf{s}^e
\end{aligned} \tag{2.20}$$

Last equation shows that $\mathbf{s}_{n+1}$ is co-linear with $\mathbf{s}^e$. Therefore,

$$\mathbf{N}_{n+1} = \frac{3}{2\sigma_e|_{n+1}}\mathbf{s}_{n+1} = \frac{3}{2\sigma^e_e}\mathbf{s}^e \equiv \mathbf{N}^e = known \tag{2.21}$$

By taking the dot product of equation (2.20) with $\mathbf{N}_{n+1} = \mathbf{N}^e$, $\sigma_e(\bar{\varepsilon}^p)$ is calculated:

$$\underbrace{\mathbf{s}_{n+1} : \mathbf{N}_{n+1}}_{\sigma_e|_{n+1}} = \underbrace{\mathbf{s}^e : \mathbf{N}^e}_{\sigma^e_e} - 2G\Delta\bar{\varepsilon}^p \underbrace{\mathbf{N}_{n+1} : \mathbf{N}_{n+1}}_{3/2} \;\Rightarrow\; \sigma_e|_{n+1} = \sigma^e - 3G\Delta\bar{\varepsilon}^p \tag{2.22}$$

Then, the yield condition (2.10) becomes:

$$F(\Delta\bar{\varepsilon}^p) = \sigma^e_e - 3G\Delta\bar{\varepsilon}^p - \sigma_y(\bar{\varepsilon}^p_n + \Delta\bar{\varepsilon}^p, C_L|_{n+1}) = 0 \tag{2.23}$$

During the solution in a finite element setting $C_L|_{n+1}$ is known and equation (2.23) suggests a non-linear equation for $\Delta\bar{\varepsilon}^p$. The above equation is solved by using Newton's method. A

first estimate for the method could be found by approximating last equation as:

$$\sigma_e^e - 3G\Delta\bar{\varepsilon}^p - \left[\sigma_y\left(\bar{\varepsilon}_n^p, C_L\big|_{n+1}\right) + \underbrace{\left.\frac{\partial\sigma_y\left(\bar{\varepsilon}^p, C_L\big|_{n+1}\right)}{\partial\bar{\varepsilon}^p}\right|_{\bar{\varepsilon}^p=\bar{\varepsilon}_n^p}}_{h}\Delta\bar{\varepsilon}^p\right] = 0 \Rightarrow$$

$$\Delta\bar{\varepsilon}^p = \frac{\sigma_e^e - \sigma_y\left(\bar{\varepsilon}^p, C_L|_{n+1}\right)}{3G+h} \tag{2.24}$$

After $\Delta\bar{\varepsilon}^p$ has been found, $\mathbf{s}_{n+1}$ can determined from equation (2.20), i.e, $\mathbf{s}_{n+1} = \mathbf{s}^e - 2G\Delta\bar{\varepsilon}^p\mathbf{N}_{n+1}$ is known. Also, p_{n+1} is determined from equation (2.17) or equation (2.18). The Jacobian for the Newton loop is:

$$J = \frac{\partial F(\Delta\bar{\varepsilon}^p)}{\partial\Delta\bar{\varepsilon}^p} = -3G - \frac{\partial\sigma_y}{\partial\bar{\varepsilon}^p}. \tag{2.25}$$

2.3 Heat transfer analogy

Because of the limited flexibility offered by mass diffusion analysis in Finite Element commercial software, certain authors have resorted to drawing an analogy between heat transfer and diffusion as a means to numerically implement their methods. In order to solve the coupled stress-diffusion constitutive model, this analogy is used. Transport phenomena

Table 2.1: Analogy of variables between heat transfer and diffusion analysis in ABAQUS

Heat equation		**Mass diffusion equation**
Temperature: T	$\rightarrow$	Lattice Hydrogen Concentration: C_L
Internal Energy: U	$\rightarrow$	Total Hydrogen Concentration: C_{total}
Heat Flux: $\mathbf{q}$	$\rightarrow$	Hydrogen Flux: $\mathbf{J}$
Heat Source Term: $\dot{r}$	$\rightarrow$	0
Density : ρ	$\rightarrow$	1

are characterized by analogous balance equations and fluxes. Specifically, the exchange of momentum is scrutinized in viscous fluids, while heat transfer analysis focuses on energy exchange, and diffusion processes deal with the exchange of mass [18]. In the utilization of ABAQUS, various subroutines are customarily developed. Table 2.1 provides a summary of the correspondence between the heat equation and the hydrogen diffusion equation. The coupled thermo-mechanical procedure available in ABAQUS can be effectively employed to address coupled diffusion-mechanics problems.

2.3.1 Model implementation in ABAQUS

To implement the diffusion constitutive equations, the UMATHT and VUMATHT user subroutines have been utilized in ABAQUS/Standard and ABAQUS/Explicit, respectively. The energy balance is expressed as follows:

$$\int_{\Omega} \rho U dV = \int_{\Omega} r dV + \int_{\partial\Omega} -\mathbf{q}\cdot\mathbf{n} dS \;\Rightarrow\; \int_{\Omega} (\rho U + \nabla\cdot\mathbf{q} - r) dV = 0 \;\; \forall\Omega \;\Rightarrow\; \boxed{\rho U + \nabla\cdot\mathbf{q} = r} \tag{2.26}$$

where r is the heat source per unit volume (J/m^3) and depends on the temperature gradient according to Fourier's law, U is the internal energy per unit mass and q is the heat flux per unit area (W/m^2). Setting the density equal to one, total hydrogen concentration might be regarded as the internal energy per unit mass. Note that $-\mathbf{q}\cdot\mathbf{n} \equiv r$ is the thermal power entering Ω per unit area. It should be noted that when the material is plastically incompressible then:

$$J = J_0 \det(\mathbf{F}) = J_0 \det(\mathbf{F}^e) = J_0\Big(1 + O(\epsilon)\Big) \approx J_0 \quad \text{and} \quad \rho = \frac{\rho_0}{J} \approx \rho_0 \tag{2.27}$$

where $F_{ij} = \partial x_i/\partial X_j$ is the deformation gradient and ρ_0, ρ are the densities with respect to the initial and current configurations respectively. By taking this result into account, equation (2.26) can be written as:

$$\boxed{\rho_0 U + \nabla\cdot\mathbf{q} \approx r} \quad \text{or} \quad \boxed{\rho U + \nabla\cdot\mathbf{q} \approx r} \tag{2.28}$$

For the hydrogen diffusion, in the mass conservation equation (2.2), $-\mathbf{J}\cdot\mathbf{n} \equiv J_n$ is analogous to $-\mathbf{q}\cdot\mathbf{n} \equiv r$. In UMATHT, material properties are calculated based on input parameters. The constitutive equations are of the form:

$$\mathbf{J}(C_L, \nabla C_L, \nabla p) = -D\nabla C_L + \frac{DV_H}{RT} C_L \nabla p, \tag{2.29}$$

$$C_T(C_L, \bar{\varepsilon}^p) = \alpha\theta_T(C_L) N_T(\bar{\varepsilon}^p), \tag{2.30}$$

$$\theta_T(C_L) = \frac{K_T\theta_L(C_L)}{1 + K_T\theta_L(C_L) - \theta_L(C_L)}, \;\; \frac{1}{\theta_T(C_L)} = 1 + \left[\frac{1}{\theta_L(C_L)} - 1\right]\frac{1}{K_T}, \tag{2.31}$$

$$\theta_L(C_L) = \frac{C_L}{\beta N_L} \tag{2.32}$$

Details for the calculation of the pressure gradient are given in Appendix A For given $(\bar{\varepsilon}^p, C_L, \nabla C_L, \nabla p)$, $(U, \mathbf{q})$ and the corresponding Jacobians are defined as :

$$C_T = C_T(C_L, \bar{\varepsilon}^p), \quad U(C_L, \bar{\varepsilon}^p) = C_L + C_T(C_L, \bar{\varepsilon}^p), \tag{2.33}$$

$$\frac{\partial U}{\partial T} = 1 + \frac{\partial C_T}{\partial C_L}, \quad \frac{\partial U}{\partial \nabla T} = \frac{\partial U}{\partial \nabla C_L} = 0, \tag{2.34}$$

where

$$\frac{\partial C_T}{\partial C_L} = \alpha \frac{\partial \theta_T}{\partial C_L} N_T, \quad \frac{\partial \theta_T}{\partial C_L} = \frac{K_T}{(1 + K_T\theta_L - \theta_L)^2} \frac{\partial \theta_L}{\partial C_L}, \quad \frac{\partial \theta_L}{\partial C_L} = \frac{1}{\beta N_L}, \tag{2.35}$$

$$\mathbf{q}(\nabla C_L, C_L, \nabla p) = \mathbf{J}(C_L, \nabla C_L, \nabla p), \quad \frac{\partial \mathbf{q}}{\partial T} = \frac{\partial \mathbf{J}}{\partial C_L} = \frac{DV_H}{RT}\nabla p, \quad \frac{\partial \mathbf{q}}{\partial \nabla T} = \frac{\partial \mathbf{J}}{\partial \nabla C_L} = -D\boldsymbol{\delta}. \tag{2.36}$$

It should be noted that in this case, the variable U depends not only on temperature (i.e, lattice concentration) but also on the displacement field $\mathbf{u}$ through dependence on the equivalent plastic strain $\bar{\varepsilon}^p(\mathbf{u}, C_L)$. Additionally, the variable $\mathbf{q}$ is dependent on $\mathbf{u}$ due to the relationship with ∇p. It's worth noting that ABAQUS lacks the capability to directly compute $\frac{\partial U}{\partial \boldsymbol{\Delta}\varepsilon}$ and $\frac{\partial \mathbf{q}}{\partial \nabla p}$, which means that the Jacobian matrix within the global ABAQUS Newton loop is not precisely determined. As a result, this may necessitate the use of small incremental steps to achieve convergence.

Chapter 3

Applications and Results

In this study, hydrogen diffusion is influenced by both hydrostatic stress and plastic straining, primarily through trapping mechanisms. The analysis is conducted for a body-centered cubic (BCC) iron system. Trap characteristics of this system are establish based on the work of Taha and Sofronis [19]. More specifically, the trap binding energy is $\Delta H_B = -60\ KJ\ mol^{-1}$ and is independent of temperature and the amount of plastic deformation. Their findings also indicate that trap densities remain constant regardless of temperature, increase significantly with deformation at lower deformation levels, and then exhibit a more gradual increase with further deformation. In line with these experimental observations, the trap density N_T varies with the equivalent plastic strain $\bar{\varepsilon}^p$, as illustrated in Figure 3.1.

$$\log_{10} N_T\left(\bar{\varepsilon}^p\right) = 23.26 - 2.33e^{-5.5\bar{\varepsilon}^p} \tag{3.1}$$

Alternative expressions for the trap density as a function of the accumulated plastic strain

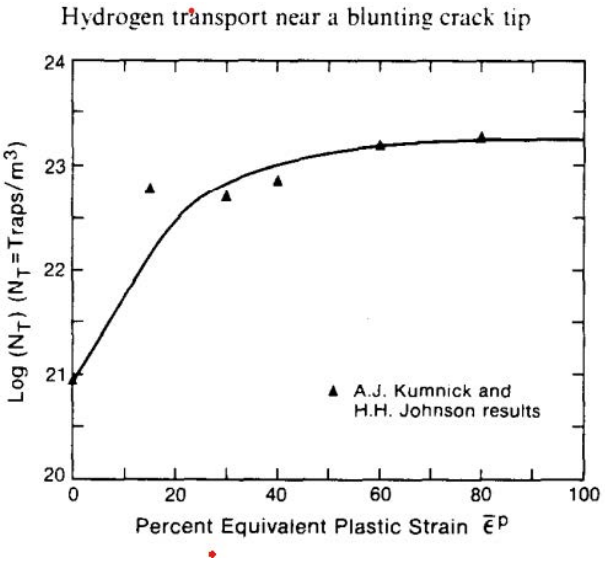

Figure 3.1: A proposed relationship between N_T and $\bar{\varepsilon}^p$ [20].

can be found in the literature. In one such expression, trap sites are linked with dislocations within the deforming metal. Assuming one trap site per atomic plane affected by a dislocation, the trap site density, measured in traps per cubic meter, can be determined as follows:

$$N_T = \sqrt{2}\rho/\alpha \tag{3.2}$$

where ρ^d is the dislocation density and α is the lattice parameter. According to Lufrano [21], this assumption aligns with the experimental findings of Thomas [22], where the optimal fit to the experimental data was achieved with a trapping radius of only 1 to 2 atomic spacings. The dislocation density, denoted as ρ^d and measured in dislocation line length per cubic meter, was observed to vary linearly with equivalent plastic strain $\bar{\varepsilon}^p$:

$$\rho^d = \begin{cases} \rho_0^d + \gamma\bar{\varepsilon}^p & \text{if } \bar{\varepsilon}^p < 0.5 \\ 10^{16} & \text{if } \bar{\varepsilon}^p \geq 0.5 \end{cases} \tag{3.3}$$

where $\rho_0^d = 10^{10}$ line length$/m^3$ denotes the dislocation density for the annealed material and $\gamma = 2.0 \times 10^{16}$ line length$/m^3$ [17]. In all calculations that follow, we use the trap density that is given by equation (3.1).

The parameter α in (1.3) and the parameter β in (1.1) were considered to have a value of 1. Moreover, the molar volume of iron is $V_M = 7.116 \times 10^{-6}\ m^3\ mol^{-1}$ and so (1.2) gives $N_L = 8.4643 \times 10^{28}$ iron lattice atoms per cubic meter. It is generally assumed that interstitial hydrogen causes an isotropic expansion of the lattice, with its partial molar volume in a solution being equal to $\bar{V} = 2.0 \times 10^{-6}\ m^3\ mol^{-1}$. The lattice diffusion constant for hydrogen at 300K was measured as $D = 1.27 \times 10^{-8} m^2/s$. Sievert's law provides the hydrogen stress-free equilibrium solubility as a function of environmental pressure and temperature, particularly for temperatures significantly exceeding 300 K [23].

$$C_L = 1.989 \times 10^{26} \sqrt{p \exp\Big(-\frac{\Delta\bar{H}_s}{RT}\Big)} \tag{3.4}$$

where C_L is atoms of H_2 gas per m^3 of iron under normal conditions of pressure and temperatures, p is the hydrogen pressure in atmospheres and $\Delta\bar{H} = 28.6\ KJ\ mol^{-1}$ is the heat of solution [24]. The mechanical and diffusion properties are presented in Tables 3.1 and 3.2 as outlined in [19]. The model developed in Chapter 2 was used to simulate the problem

Table 3.1: Mechanical Properties

E(GPa)	ν	σ_0(MPa)	Hardening Exponent (n)
207	0.3	250	5

of Mode-I fracture of a blunting crack under plane strain and small scale yielding conditions in the presence of hydrogen. It should be noted that in the context of this work a "one-way

Table 3.2: Diffusion Properties

$D\left(\frac{m^2}{s}\right)$	$V_H\left(\frac{m^3}{mol}\right)$	K_T	$N_L\left(\frac{Fe\ atoms}{m^3}\right)$	λ	α	β
1.27×10^{-8}	2×10^{-6}	2.8×10^{10}	8.46×10^{28}	0.281	1	1

coupling" effect was assumed; put it simply, only the effect of the stress fields on hydrogen diffusion were accounted for while it was assumed that hydrogen distribution does not affect the flow stress of the material.

Two different situations were examined regarding the hydrogen boundary conditions at the crack surface (see [1]). In the first case, which corresponds to the problem of "environmental embrittlement", the material is considered to be at a specific temperature surrounded by gaseous hydrogen at the same temperature T and pressure p. In the following, this type of boundary condition will be referred to as the "constant concentration" boundary condition. In the second case, which corresponds to the problem of "internal embrittlement", all external surfaces are assumed to be insulated. In the situation of an insulated crack surface, the primary transport phenomenon is dominated by the diffusion of hydrogen within the solid material. In the following, this type of boundary condition will be referred to as the "zero flux" boundary condition. Initially, in both cases, the stress-free solid is in equilibrium with the hydrogen gas, resulting in uniform NILS concentrations and $C_L|_{t=0} = C_0$ is established everywhere given by (1.6). The corresponding initial concentration in trapping sites, denoted as $C_T|_{t=0}$, is derived from the population of NILS according to equation (1.3).

At the starting point ($t = 0$), loads are applied and then progressively increased to levels where the crack opening displacement size is significantly expanded, reaching several times its initial size. Our focus is on situations involving local yielding in the plane strain condition, where the plastic zone is confined to a region around the crack tip. As will be shown at the end of Section 3.2, we conclude that the size of the plastic zone is deemed negligible relative to the size of the solution domain. This ensures that small-scale yielding conditions persist, the boundary layer approach remains valid, and the finite geometry material can be replaced with an infinite body containing a semi-infinite crack while applying asymptotic boundary conditions. The conditions are applied incrementally to enforce the Mode-I plane strain elastic asymptotic solution and are of the form:

$$\begin{Bmatrix} u_1^I \\ u_2^I \end{Bmatrix} = \frac{K_I}{2\mu}\sqrt{\frac{r}{2\pi}}(3 - 4\nu - \cos\theta) \begin{Bmatrix} \cos(\frac{\theta}{2}) \\ \sin(\frac{\theta}{2}) \end{Bmatrix} \tag{3.5}$$

where u_i^I with $i = 1, 2$ is the displacement field, K_I is the stress intensity factor from the solution of the linear elastic crack problem, ν is the Poisson ratio of the material and r and θ are polar coordinates. Utilizing symmetry enables the modeling of both diffusion and elastic-plastic behavior within the two-dimensional region, where the angle θ ranges from 0 to π. As a result, along the symmetry line where $\theta = 0$, there are no shear tractions and no

displacements in the y-direction. Additionally, the hydrogen flux across this symmetry line is zero. Proper normalization of the governing equations leads to the following form for the solution of the coupled boundary value problem:

$$\frac{\mathbf{u}}{\ell} = \mathbf{f}\left(\frac{\mathbf{x}}{\ell}, \frac{t}{t_0}, \frac{E}{\Sigma_0}, \nu, \frac{\sigma_0}{\Sigma_0}, \varepsilon_0, n, K_T, \frac{N_L}{C_0}, \lambda, \frac{D}{\ell^2/t_0}, \frac{V_H}{RT/\Sigma_0}\right) \tag{3.6}$$

$$\frac{\boldsymbol{\sigma}}{\Sigma_0} = \mathbf{g}\left(\frac{\mathbf{x}}{\ell}, \frac{t}{t_0}, \frac{E}{\Sigma_0}, \nu, \frac{\sigma_0}{\Sigma_0}, \varepsilon_0, n, K_T, \frac{N_L}{C_0}, \lambda, \frac{D}{\ell^2/t_0}, \frac{V_H}{RT/\Sigma_0}\right) \tag{3.7}$$

$$\frac{C_L}{C_0} = m\left(\frac{\mathbf{x}}{\ell}, \frac{t}{t_0}, \frac{E}{\Sigma_0}, \nu, \frac{\sigma_0}{\Sigma_0}, \varepsilon_0, n, K_T, \frac{N_L}{C_0}, \lambda, \frac{D}{\ell^2/t_0}, \frac{V_H}{RT/\Sigma_0}\right) \tag{3.8}$$

$$\frac{\mathbf{J}}{C_0 l/t_0} = s\left(\frac{\mathbf{x}}{\ell}, \frac{t}{t_0}, \frac{E}{\Sigma_0}, \nu, \frac{\sigma_0}{\Sigma_0}, \varepsilon_0, n, K_T, \frac{N_L}{C_0}, \lambda, \frac{D}{\ell^2/t_0}, \frac{V_H}{RT/\Sigma_0}\right) \tag{3.9}$$

Proper normalization is used for all properties related to both the mechanical and the diffusion problem. To be precise, Young's modulus E, initial yield stress σ_0, number of solvent lattice atoms per unit volume N_L, diffusion coefficient D, and the partial molar volume of hydrogen V_H are all normalized in the pre-processing stage; the trap density function N_T is normalized in the user subroutine code. The corresponding normalized quantities are defined as follows:

$$\hat{E} = \frac{E}{\Sigma_0}, \quad \hat{\sigma_0} = \frac{\sigma_0}{\Sigma_0}, \quad \hat{N_L} = \frac{N_L}{C_0}, \quad \hat{D} = \frac{D}{\ell^2/t_0}, \quad \hat{V_H} = \frac{V_H}{RT/\Sigma_0}, \quad \text{and} \quad \hat{N_T} = \frac{N_T}{C_0} \tag{3.10}$$

The values of the normalizing parameters used in all calculations are summarized in Table 3.3.

Table 3.3: Normalizing parameters

$\ell\left(m\right)$	$t_0\left(s\right)$	$C_0\left(H\ atoms/m^3\right)$	$R\left(J/mol \cdot K\right)$	$T\left(K\right)$	$\Sigma_0\left(Pa\right)$
5×10^{-6}	1	2.086×10^{21}	8.314	300	250×10^6

The meshes that were used in the near tip region for the 2-dimensional simulations are shown in their undeformed configurations in Figure 3.3. The initial radius was b_0 and the radius of the outer periphery was R. Displacement boundary conditions, as specified in (3.5), were imposed at this outer radius. By implementing these boundary conditions at such a distant location from the crack tip, small-scale yielding conditions are ensured effectively. In fact, in all instances, the stress field in the far field was primarily characterized by linear elasticity. To accurately capture crack tip blunting and the impact of plasticity on hydrogen diffusion, a very fine discretization of the region surrounding the crack tip was employed. Different meshes were used for the simulations in ABAQUS/Standard and ABAQUS/Explicit. The mesh used in ABAQUS/Standard consisted of 6134 8-node plane strain, coupled temperature-displacement elements (CPE8RT) with reduced integration. The meshes used in ABAQUS/Explicit consisted of 1658 4-node plane strain, coupled temperature displacement

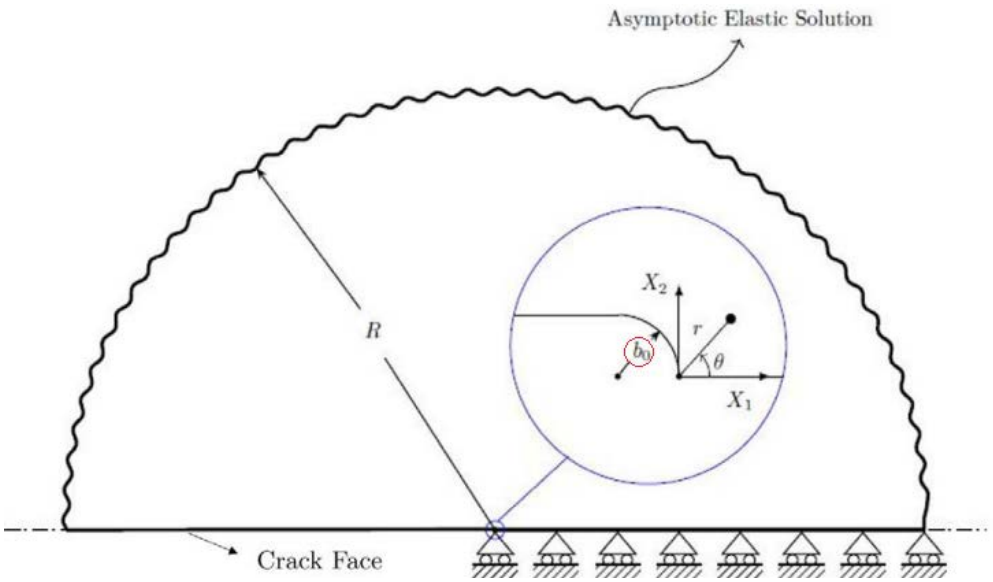

Figure 3.2: Schematic representation of geometry and boundary conditions near the crack tip. The "boundary layer" elastic solution is applied on the outer radius R and b_0 is the initial notch radius.

elements (CPE4RT) for the 2-dimensional case and 3316 8-node "brick", coupled temperature displacement elements (C3D8RT), both with reduced integration, in the 3-dimensional case.

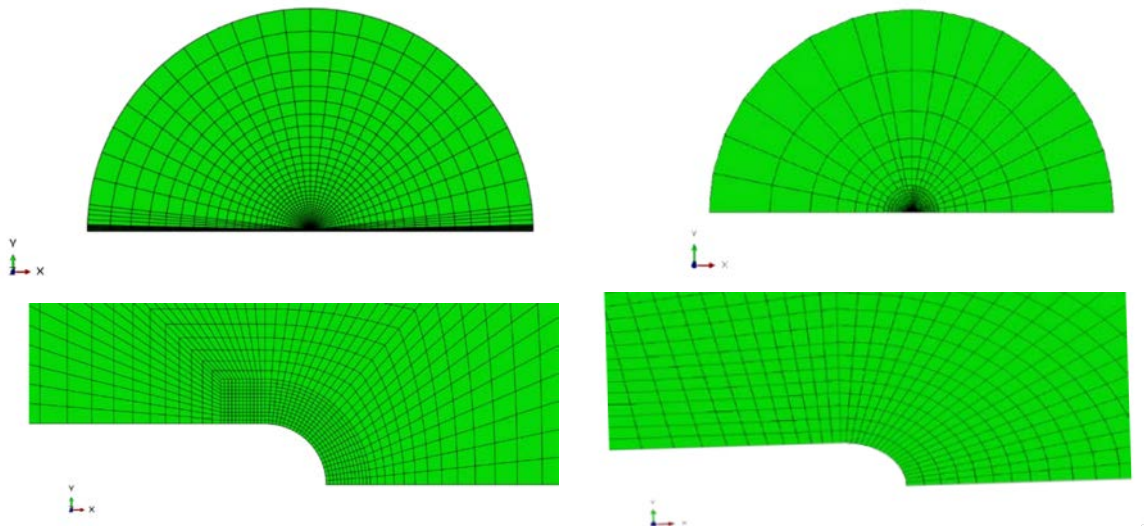

(a) ABAQUS/Standard ($R = 84000b_o$) (b) ABAQUS/Explicit ($R = 1200b_0$)

Figure 3.3: Meshes used in numerical simulations.

3.1 Simulations using ABAQUS/Standard

In the following we present the results from the simulation of the problem described in the previous section using ABAQUS/Standard. The results were found to be in good agreement with those presented by Taha and Sofronis in [19]. The loads and boundary conditions applied are outlined in Table 3.4. The results from the simulations in ABAQUS/Standard

Table 3.4: Loads and boundary conditions for the Mode-I fracture problem with hydrogen diffusion.

Load Level	$22.425MPa\sqrt{m}$
Total Time	32.5 s
Constant Concentration B.C	$C_L^{Crack\ Face} = C_0$
Zero Flux B.C	$\mathbf{J^{Crack\ Face} = 0}$

are presented in Figures 3.4-3.10. In all cases, $x/(K_I/\sigma_0)^2$ is the normalized distance along the axis of symmetry in front of the crack tip. Figure 3.4 displays the equivalent plastic strain, relative to the normalized distance from the undeformed configuration's notch root. In addition, the normalized hydrogen distribution at trapping sites C_T/C_0 at the conclusion of the loading process is shown in Figure 3.5. The site of accumulation of trapped hydrogen is near the crack surface and the profile of the concentration C_T follows closely that of the plastic strain in Figure 3.4. This is because the trap density increases monotonically with plastic strain as shown in Figure 3.1. Hydrogen diffusion through NILS effectively delivers hydrogen to trapping sites at a rate that exceeds the rate associated with high binding energy. Consequently, once the loading process stops and plastic straining no longer generates traps, there is minimal alteration in the trapped hydrogen concentration. As a result, the trapped hydrogen concentrations stabilize once the load is terminated.

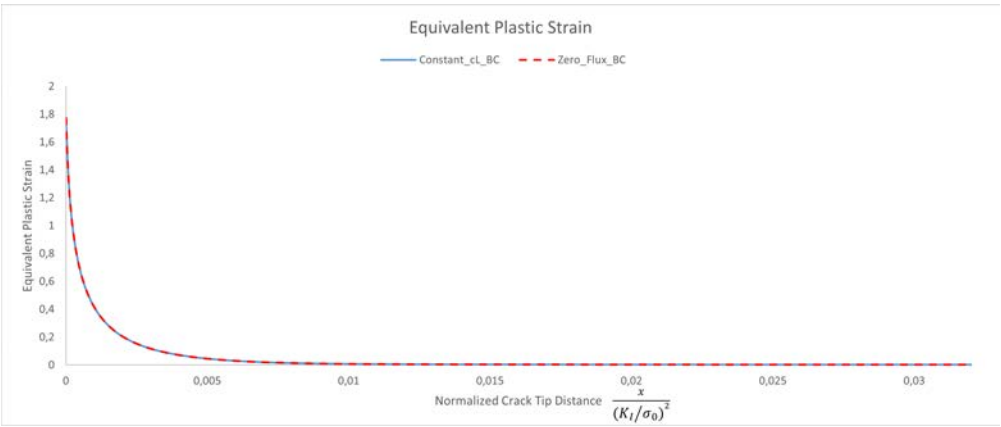

Figure 3.4: Distribution of $\bar{\varepsilon}^p$ near the crack tip.

The distribution of lattice hydrogen concentration in front of the crack tip is depicted in Figure 3.7. As it is seen, the concentration in NILS is significantly lower when compared to the corresponding hydrogen content in traps implying that the total hydrogen concentration

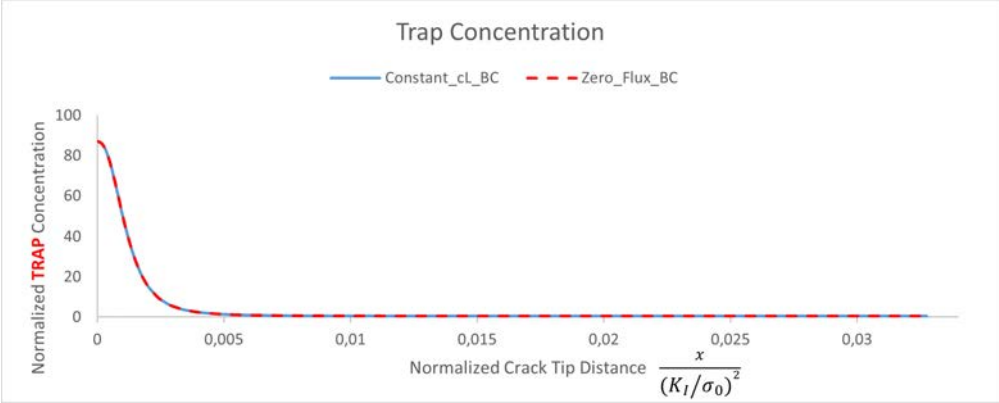

Figure 3.5: Distribution of normalized trap concentration $\frac{C_T}{C_0}$ near the crack tip.

is dominated by the content in trapping sites. Also, the profile of lattice hydrogen concentration follows that of the hydrostatic stress as shown in Figure 3.6; this is to be expected due to the dependence of hydrogen diffusion on the gradient of the hydrostatic stress, as mentioned in Chapter 2.

In case of zero flux boundary conditions, the maximum lattice hydrogen concentrations observed during straining exhibit slightly lower values $\left([C_L/C_0]_{max} \approx 1.5\right)$ compared to those seen under constant concentration boundary condition $\left([C_L/C_0]_{max} \approx 1.8\right)$. This is also shown from Figure 3.8, where the lattice concentration near the crack tip attains slightly higher values in the case of constant boundary condition. Under zero flux boundary conditions, the requirements for filling traps with hydrogen at the crack surface and supplying hydrogen to the high-stress region in NILS are solely met by the diffusion of hydrogen from the bulk of the specimen, located far from the crack tip, toward the crack tip itself. In simpler terms, the extra supply of hydrogen through the crack surface, which was present under constant concentration boundary conditions, is absent in the insulated specimen. As a result, the lattice sites in the insulated specimen experience more depletion because there is a reduced amount of hydrogen available from NILS for distribution. It should be mentioned that in contrast to the lattice concentrations, there is no alteration in the trapping concentration after straining. Therefore, any fluctuations in the total hydrogen concentration are solely a result of variations in the NILS concentration. Since the NILS populations are significantly smaller in magnitude compared to the trapped populations, the profile of the total hydrogen concentration, $C_T + C_L$, closely resembles that of the case with constant concentration boundary conditions, in which the traps were also fully saturated during straining.

3.2 Simulations using ABAQUS/Explicit

The problem of Mode-I fracture under plane strain conditions with small-scale yielding was replicated using ABAQUS/Explicit. For this purpose, 4-node bilinear elements with reduced integration were employed. Final load level and the applied boundary conditions

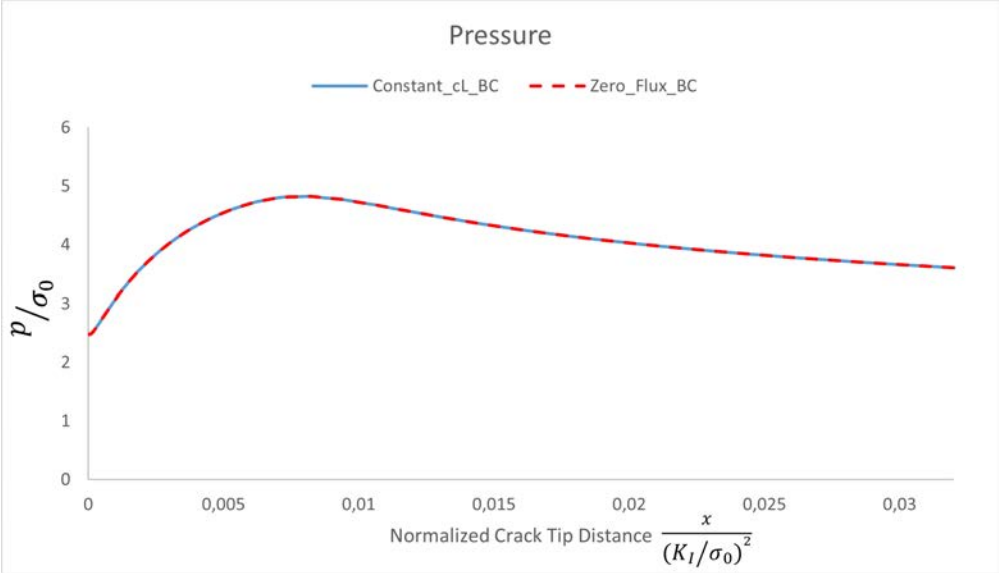

Figure 3.6: Distribution of normalized hydrostatic stress $\frac{p}{\sigma_0}$ near the crack tip.

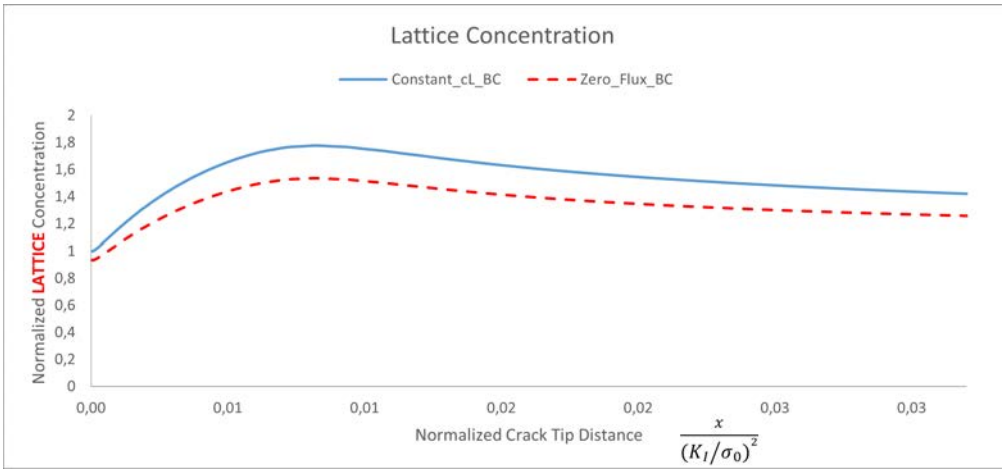

Figure 3.7: Distribution of normalized lattice concentration $\frac{C_L}{C_0}$ near the crack tip.

for the diffusion problem are presented in Table 3.5. Simulations were conducted in both

Table 3.5: Loads and boundary conditions for the Mode-I fracture problem with hydrogen effects in ABAQUS/Explicit.

Load Level	$22.425MPa\sqrt{m}$
Total Time	$32.5\ s$
Zero Flux B.C	$\mathbf{J^{Crack\ Face} = 0}$

2D and 3D settings, with appropriate boundary conditions applied. The 3D simulations were carried-out by restricting displacement in the out of plane direction (i.e., the condition $u_3 = 0$ was applied to all degrees of freedom in this case) in order to enforce plane strain conditions for a fair comparison with the two-dimensional results. It should be noted that in ABAQUS/Explicit, simulations are inherently dynamic, meaning that inertia forces are

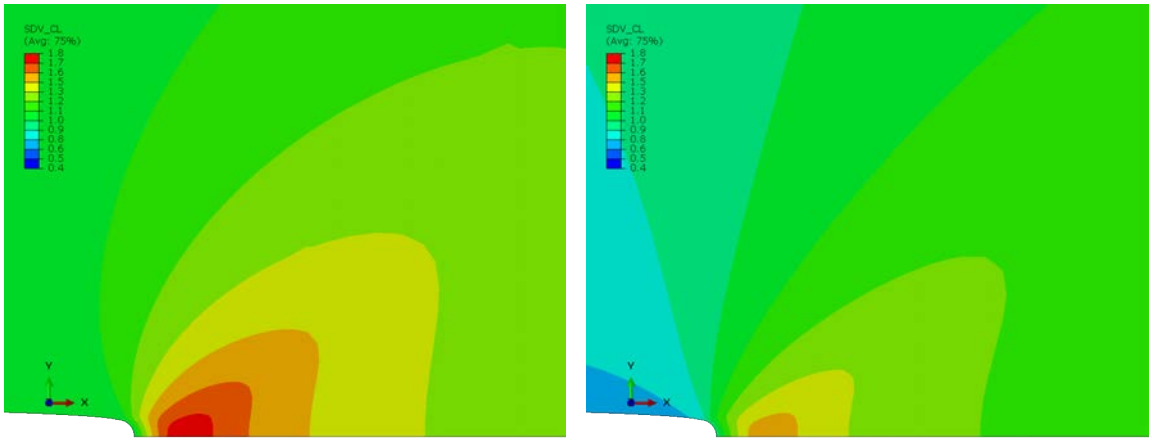

(a) Constant concentration B.C. (b) Zero flux B.C.

Figure 3.8: Contours of lattice concentration near the crack tip for the two different boundary conditions.

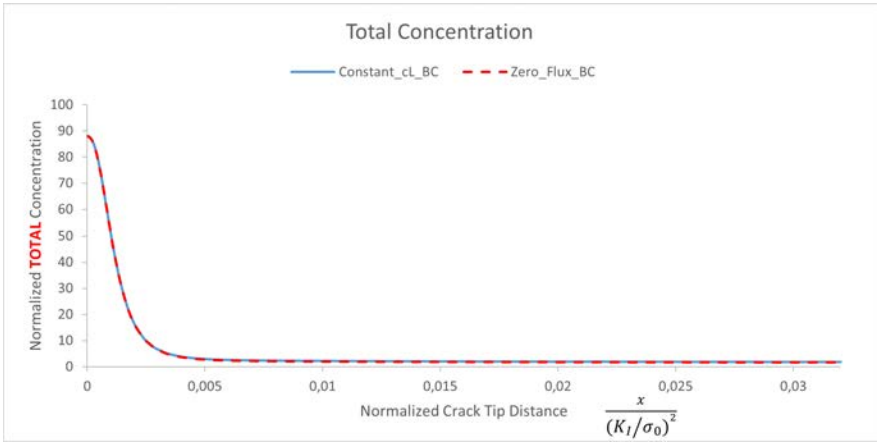

Figure 3.9: Distribution of normalized total concentration $(C_T + C_L)/C_0$ near the crack tip.

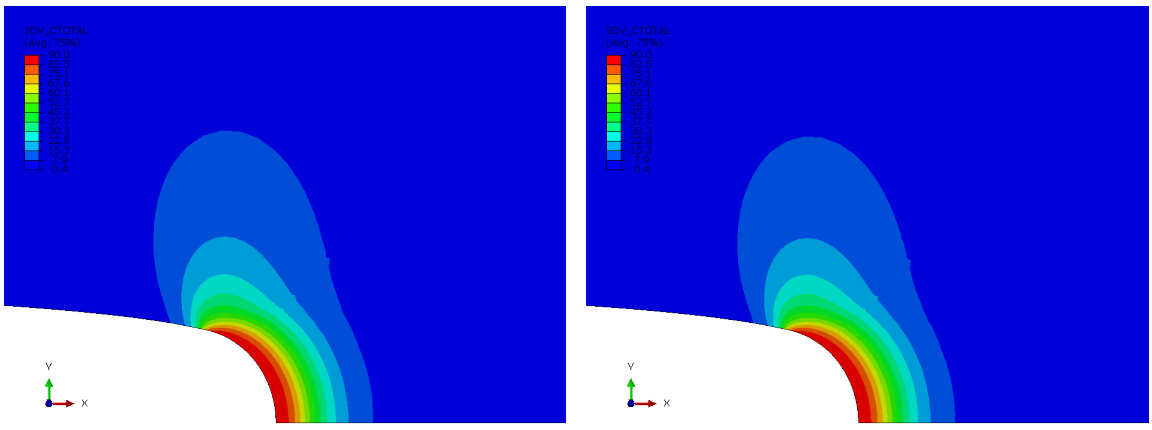

(a) Constant concentration B.C. (b) Zero flux B.C.

Figure 3.10: Contours of total concentration near the crack tip for the two different boundary conditions.

not omitted. To ensure that the simulations align with those conducted using ABAQUS/-Standard, a density parameter (ρ) is selected such that the kinetic energy does not exceed 5% of the strain energy by the conclusion of the analysis. This adjustment helps maintain equivalence between the two sets of simulations.

The results obtained from these simulations were found to be in very good agreement with the predictions made using ABAQUS/Standard. The hydrogen trap concentration for

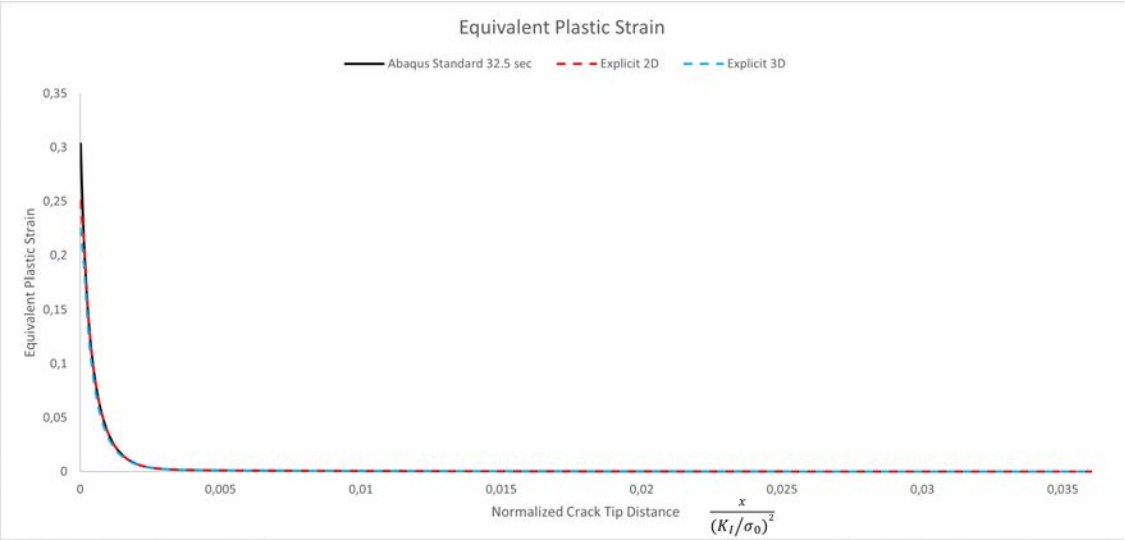

Figure 3.11: Distribution of $\bar{\varepsilon}^p$ near the crack tip.

both 2D and 3D simulations in front of the blunting crack tip is reported in Figure 3.12. In both the path and the contour plots, it appears that the trap concentration in 2D is slightly higher than in 3D. On the contrary, the maximum lattice hydrogen concentration is slightly higher for the three-dimensional model. The total hydrogen concentration is found be

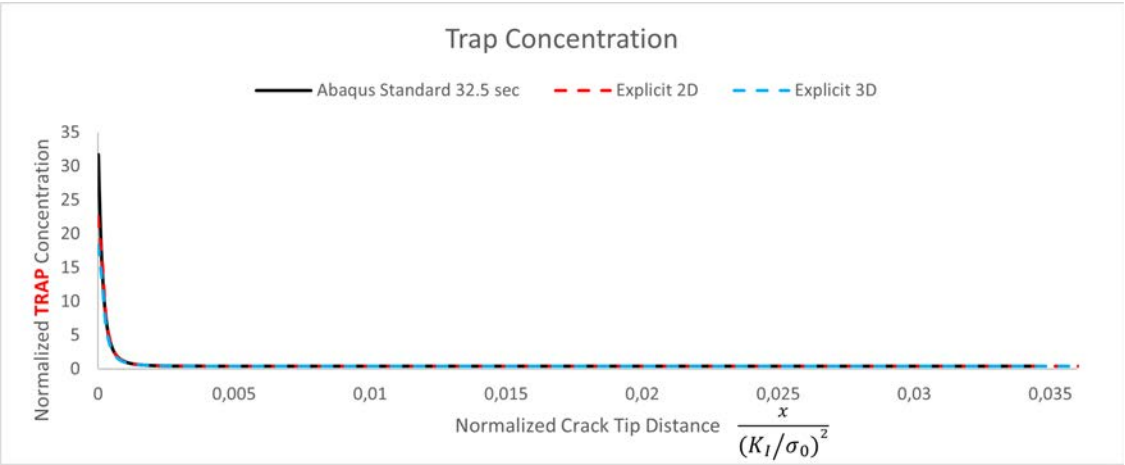

Figure 3.12: Distribution of normalized trap concentration $\frac{C_T}{C_0}$ near the crack tip.

very close to the trap concentration, as in implicit simulations. Due to the minor variations between 2D and 3D trap concentrations, there are no discernible differences in the overall concentration. Finally, as it can be seen from Figure 3.18, the plastic zones in all cases

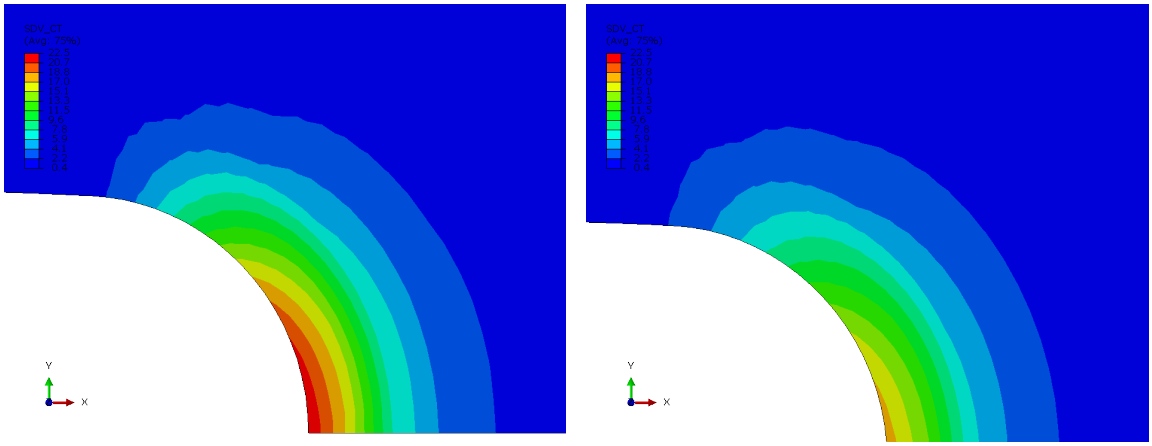

(a) 2D (b) 3D

Figure 3.13: Contours of hydrogen trap concentration near the crack tip.

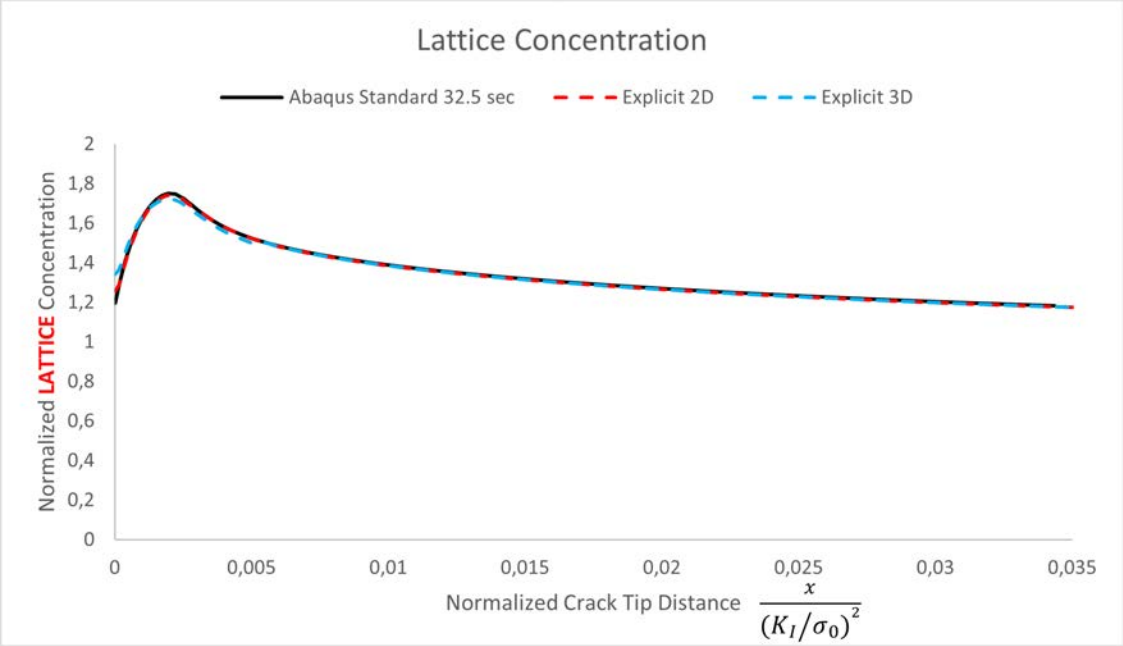

Figure 3.14: Distribution of normalized lattice concentration $\frac{C_L}{C_0}$ near the crack tip.

remain confined relative to the size of the domain under consideration verifying the small scale yielding hypothesis.

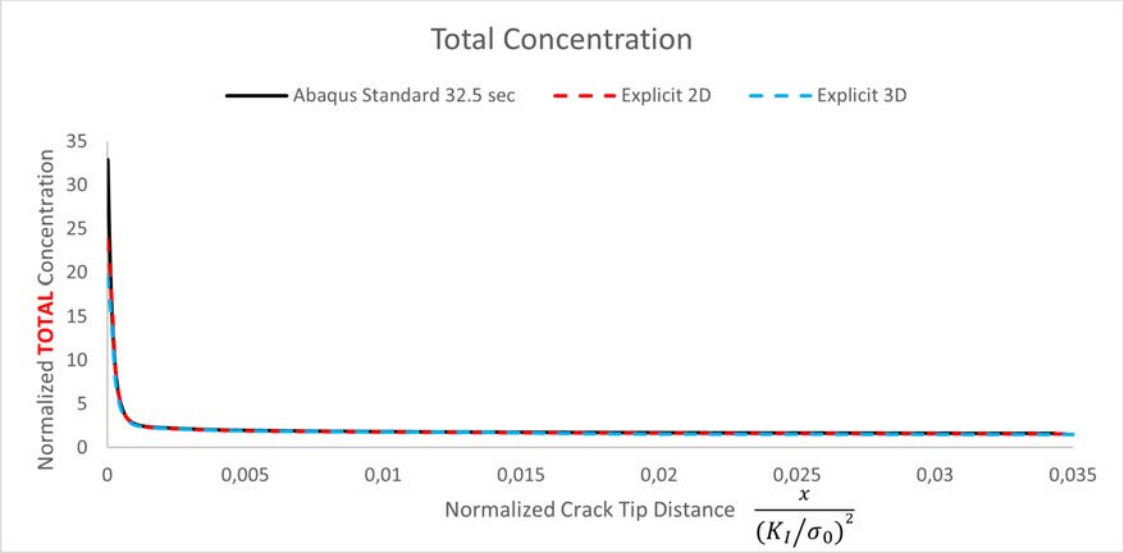

Figure 3.15: Distribution of normalized total concentration $(C_T + C_L)/C_0$ near the crack tip.

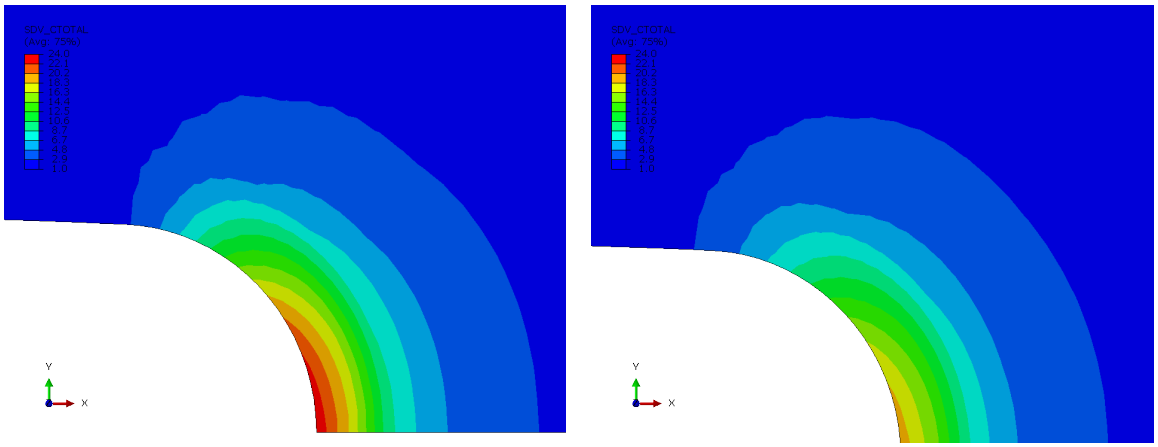

(a) 2D (b) 3D

Figure 3.16: Contours of total Concentration

Conclusions

An isotopic elastic-plastic model with hydrogen effects was used to simulate the Mode-I fracture problem in the vicinity of a blunting crack tip under small scale yielding boundary conditions. The cases of both environmental and internal embrittlement corresponding to constant hydrogen concentration and zero flux boundary conditions on the crack face were employed in the analyses. Also, to test the validity of the constitutive model's implementation, numerical calculations were carried-out using both ABAQUS/Standard and ABAQUS/Explicit.

The analyses show that the distribution of hydrogen near a crack tip is influenced by two competing mechanisms. One mechanism is the creation of traps through plastic straining, represented by concentration C_T, while the other mechanism is the effect of tensile

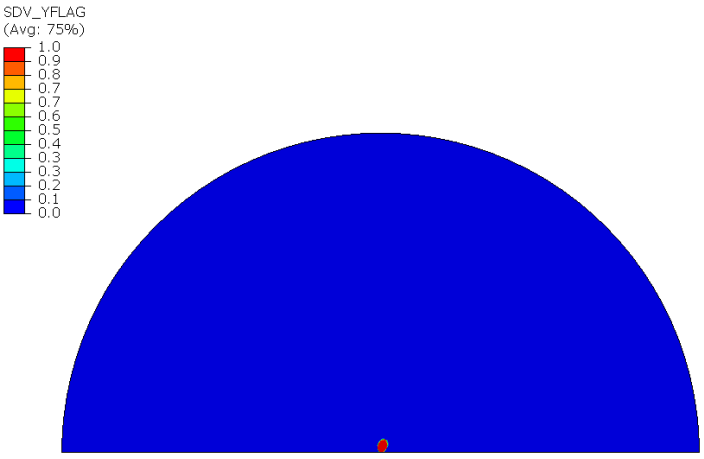

Figure 3.17: ABAQUS/Implicit

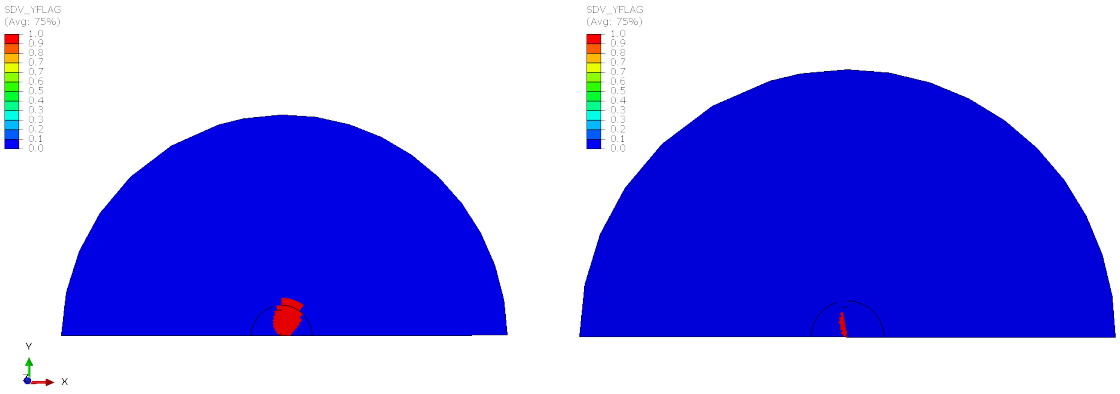

(a) ABAQUS/Explicit 2D (b) ABAQUS/Explicit 3D

Figure 3.18: Plastic Zones

hydrostatic stress, represented by concentration C_L. By applying the Oriani's equilibrium theory between the trapping site and NILS populations, it is observed that trapped hydrogen concentrations surpass NILS concentrations as plastic strain increases and the initial concentration decreases. Another significant observation from the results is the minimal contribution from the NILS concentration in this particular problem. This explains why the outcomes of the calculations are only slightly influenced by the choice of boundary conditions for the hydrogen problem. While lattice diffusion plays a role in transporting hydrogen, the presence of traps predominantly governs the hydrogen distribution. Therefore, in this particular problem, it is found that the total hydrogen concentration at the vicinity of the crack tip is dominated by the hydrogen distribution in hydrogen traps rather than the hydrogen content in the lattice.

Bibliography

[1] Sofronis, P., & McMeeking, R. M. (1989). Numerical analysis of hydrogen transport near a blunting crack tip. Journal of the Mechanics and Physics of Solids, 37(3), 317-350.

[2] Golkar, F. (2008). Study of the effect of hydrogen content on the mechanical properties in press-hardened boron steel.

[3] Wan, L., Geng, W. T., Ishii, A., Du, J.-P., Mei, Q., Ishikawa, N., Kimizuka, H., Ogata, S. (2019). Hydrogen embrittlement controlled by reaction of dislocation with grain boundary in alpha-iron, International Journal of Plasticity, 112, 206-219.

[4] Troiano, A.R. (1960). The Role of Hydrogen and Other Interstitials in the Mechanical Behavior of Metals. Transactions of the American Society of Metals, 52, 54-80.

[5] Oriani, R. A., Josephic, P. H. (1974). Equilibrium aspects of hydrogen-induced cracking of steels, Acta Metallurgica, 22(9), 1065-1074.

[6] Barrera, O., Tarleton, E., Tang, H.W., Cocks, A.C.F. (2016). Modelling the coupling between hydrogen diffusion and the mechanical behaviour of metals, Computational Materials Science, 122, 219-228.

[7] Stroe, M.E., (2006). Hydrogen embrittlement of ferrous materials. Université Libre de Bruxelles.

[8] Djukic, M.B., Bakic, G.M., Zeravcic,V.S., Sedmak, A., Rajicic, B. (2019). The synergistic action and interplay of hydrogen embrittlement mechanisms in steels and iron: Localized plasticity and decohesion, Engineering Fracture Mechanics, 216, 106528.

[9] Beachem, C.D. (1972). A new model for hydrogen-assisted cracking (hydrogen "embrittlement"). Metallurgical and Materials Transactions B, 3, 441-455.

[10] Johnson, H.H., Morlet, J., Troiano, A.R. (1958). Hydrogen, crack initiation, and delayed failure in steel, Trans. Met. Soc. AIME, 212.

[11] Hortlund, H. (2009). Study of the hydrogen diffusion out of press hardened boron steel.

[12] Hirth, J.P. (1977). Stress Corrosion Cracking and Hydrogen Embrittlement of Iron BaSE Alloys, NACE 5, 1

[13] Hashimoto, M., Latanision, R.M. (1987). The Role of Hydrogen Transport in Hydrogen Embrittlement, Springer, Dordrecht, 505-537.

[14] Bastien, P., Azou, P. (1951). Influence de l'amplitude et de la vitesse des déformations plastiques sur la ségrégation de l'hydrogène dans le fer et les aciers, Compte-rendus de l'Académie des Sciences, 1845-1848.

[15] Frank, R.C. (1959). Internal Stress and Fatigue in metals. In Proceedings of the symposium on internal stress and fatigue in metals, 411.

[16] Elmukashfi, E., Tarleton, E., Cocks, A.C.F. (2020). A modelling framework for coupled hydrogen diffusion and mechanical behaviour of engineering components. Comput Mech 66, 189-220.

[17] Sofronis, P., Liang, Y., & Aravas, N. (2001). Hydrogen induced shear localization of the plastic flow in metals and alloys. European Journal of Mechanics, A/Solids, 20(6), 857-872.

[18] Bird, R.B., Stewart, W.E., Lightfoot, E.N. (2007) Transport phenomena, New York: John Wiley Sons.

[19] Taha, A., Sofronis, P. (2001). A micromechanics approach to the study of hydrogen transport and embrittlement. Engineering Fracture Mechanics, 68(6), 803-837.

[20] Kumnick, A.J., Johnson, H.H. (1980). Deep trapping states for hydrogen in deformed iron, Acta Metallurgica, 28(1), 33-39.

[21] Lufrano, J., Sofronis, P., Symons, D. (1998). Hydrogen transport and large strain elastoplasticity near a notch in alloy X-750. Engineering Fracture Mechanics, 59(6), 827-845.

[22] Thomas, G.J. (1980). Hydrogen trapping in FCC metals (No. SAND-80-8656; CONF-800850-3). Sandia National Labs., Livermore, CA (USA), 77-85.

[23] Johnson, H.H. (1974). Hydrogen in Metals, ASM, Ohio.

[24] Hirth, J.P. (1980). Effects of hydrogen on the properties of iron and steel. Metall Trans A 11, 861-890.

.

Appendicies

Appendix A

Calculation of ∇p

A.1 Calculation for 8-node quadratic elements

This following analysis is based on the work of Barrera [6] for the calculation of the pressure gradient in the case 8-node quadratic plane elements with reduced integration (i.e, with 2×2 total integration points) in 2-dimensions. The derivatives of shape functions and the Jacobian matrix are given in this case as:

$$\Big[B\Big] = \begin{bmatrix} \frac{\partial N_1}{\partial \xi} & \frac{\partial N_2}{\partial \xi} & \frac{\partial N_3}{\partial \xi} & \frac{\partial N_4}{\partial \xi} \\ \frac{\partial N_1}{\partial \eta} & \frac{\partial N_2}{\partial \eta} & \frac{\partial N_3}{\partial \eta} & \frac{\partial N_4}{\partial \eta} \end{bmatrix} \tag{A.1}$$

$$\Big[J\Big] = \begin{bmatrix} \frac{\partial x_1}{\partial \xi} & \frac{\partial x_1}{\partial \eta} \\ \frac{\partial x_2}{\partial \xi} & \frac{\partial x_2}{\partial \eta} \end{bmatrix} \quad \Rightarrow \quad \Big[J\Big]^{-1} = \frac{1}{det([J])} \begin{bmatrix} \frac{\partial y}{\partial \eta} & -\frac{\partial x}{\partial \eta} \\ -\frac{\partial y}{\partial \xi} & \frac{\partial x}{\partial \xi} \end{bmatrix} = \begin{bmatrix} J_{11}^{-1} & J_{12}^{-1} \\ J_{21}^{-1} & J_{22}^{-1} \end{bmatrix} \tag{A.2}$$

The pressure gradient with respect to the global Cartesian coordinate system can then be calculated as:

$$\nabla p = \frac{\partial p}{\partial x_j} = \frac{\partial p}{\partial \xi_i} \frac{\partial \xi_i}{\partial x_j} = \frac{\partial p}{\partial x i_i} J_{ij}^{-1} \tag{A.3}$$

$$p = \sum_{a=1}^{4} N_a p_a \Rightarrow \frac{\partial p}{\partial \xi_i} = \sum_{a=1}^{4} \frac{\partial N_a}{\partial \xi_i} p_a = \frac{\partial N_1}{\partial \xi_i} p_1 + \frac{\partial N_2}{\partial \xi_i} p_2 + \frac{\partial N_3}{\partial \xi_i} p_3 + \frac{\partial N_4}{\partial \xi_i} p_4 \tag{A.4}$$

where $(x_1, x_2) \equiv (x, y)$ and $(\xi_1, \xi_2) \equiv (\xi, \eta)$ and p_a, $a = 1, \cdots, 4$, are the integration point pressures. Then from equations A.3 and A.4 one has:

$$\begin{aligned} \frac{\partial p}{\partial x_j} &= \left(\frac{\partial N_1}{\partial \xi_i} p_1 + \frac{\partial N_2}{\partial \xi_i} p_2 + \frac{\partial N_3}{\partial \xi_i} p_3 + \frac{\partial N_4}{\partial \xi_i} p_4 \right) J_{ij}^{-1} \\ &= \frac{\partial N_1}{\partial \xi_i} J_{ij}^{-1} p_1 + \frac{\partial N_2}{\partial \xi_i} J_{ij}^{-1} p_2 + \frac{\partial N_3}{\partial \xi_i} J_{ij}^{-1} p_3 + \frac{\partial N_4}{\partial \xi_i} J_{ij}^{-1} p_4 \\ &= \left(\frac{\partial N_1}{\partial \xi_1} J_{1j}^{-1} + \frac{\partial N_1}{\partial \xi_2} J_{2j}^{-1} \right) p_1 + \left(\frac{\partial N_2}{\partial \xi_1} J_{1j}^{-1} + \frac{\partial N_2}{\partial \xi_2} J_{2j}^{-1} \right) p_2 \end{aligned}$$

$$
\begin{aligned}
&+\left(\frac{\partial N_3}{\partial \xi_1}J_{1j}^{-1}+\frac{\partial N_3}{\partial \xi_2}J_{2j}^{-1}\right)p_3+\left(\frac{\partial N_4}{\partial \xi_1}J_{1j}^{-1}+\frac{\partial N_4}{\partial \xi_2}J_{2j}^{-1}\right)p_4\\
&=\left(B_{11}J_{1J}^{-1}+B_{21}J_{2J}^{-1}\right)p_1+\left(B_{12}J_{1J}^{-1}+B_{22}J_{2J}^{-1}\right)p_2\\
&+\left(B_{13}J_{1J}^{-1}+B_{23}J_{2J}^{-1}\right)p_3+\left(B_{14}J_{1J}^{-1}+B_{24}J_{2J}^{-1}\right)p_4
\end{aligned}
\tag{A.5}
$$

Finally,

$$
\frac{\partial p}{\partial x_1}=a_1p_1+a_2p_2+a_3p_3+a_4p_4 \quad \text{and} \quad \frac{\partial p}{\partial x_2}=b_1p_1+b_2p_2+b_3p_3+b_4p_4 \tag{A.6}
$$

where

$$
\begin{aligned}
a_1&=B_{11}J_{11}^{-1}+B_{21}J_{21}^{-1} & b_1&=B_{11}J_{11}^{-1}+B_{21}J_{21}^{-1}\\
a_2&=B_{12}J_{11}^{-1}+B_{22}J_{21}^{-1} & b_2&=B_{12}J_{11}^{-1}+B_{22}J_{21}^{-1}\\
a_3&=B_{13}J_{11}^{-1}+B_{23}J_{21}^{-1} & b_3&=B_{13}J_{11}^{-1}+B_{23}J_{21}^{-1}\\
a_4&=B_{14}J_{11}^{-1}+B_{24}J_{21}^{-1} & b_4&=B_{14}J_{11}^{-1}+B_{24}J_{21}^{-1}
\end{aligned}
\tag{A.7}
$$

A.2 Calculation for 2D or 3D linear elements

In this section we present a methodology for the calculation of the pressure gradient in the case of 2- or 3-dimensional *linear* elements. In this case, an interpolation using nodal pressures is used instead of pressure values at the integration points. Let p be interpolated as follows:

$$
p\left(\mathbf{x}\right)=\sum_{i=1}^{N_n}N_i\left(\boldsymbol{\xi}\right)p_i=\sum_{i=1}^{N_n}N_i\Big(\boldsymbol{\xi}\left(\mathbf{x}\right)\Big)p_i \tag{A.8}
$$

where N_n is the total number of nodes in the element (i.e., $N_n=4$ for 2-dimensional 4-node elements and $N_n=8$ for 3-dimensional 8-node elements) and $p_i, i=1,\cdots N_n$ are the nodal pressures. The pressure gradient can then be calculated as:

$$
\frac{\partial p}{\partial x_i}=\frac{\partial p}{\partial \xi_j}\frac{\partial \xi_j}{\partial x_i}=\left(J^{-1}\right)_{ij}\frac{\partial p}{\partial \xi_j}=\left(J^{-1}\right)_{ij}\sum_{k=1}^{N_n}\frac{\partial N_k}{\partial \xi_j}p^k \tag{A.9}
$$

Last equation can be written in the following compact form:

$$
\Big\{\nabla p\Big\}=\Big[B\Big]\left\{p^N\right\} \tag{A.10}
$$

where the dimensions of the vectors $\{\nabla p\}, \{p^N\}$ and the matrix $[B]$ depend on the dimension of the problem. More specifically, in dimensional problems and for 4-node linear elements

we have:

$$\underset{2\times1}{\{\nabla p\}} = \begin{Bmatrix} \frac{\partial p}{\partial x} \\ \frac{\partial p}{\partial y} \end{Bmatrix}, \quad \underset{4\times1}{\{p^N\}} = \begin{Bmatrix} p^1 \\ p^2 \\ p^3 \\ p^4 \end{Bmatrix}, \quad \underset{2\times4}{[B]} = \underset{2\times2}{[J]^{-1}} \underset{2\times4}{[N']}, \quad \underset{2\times4}{[N']} = \begin{bmatrix} \frac{\partial N_1}{\partial \xi} & \frac{\partial N_2}{\partial \xi} & \frac{\partial N_3}{\partial \xi} & \frac{\partial N_4}{\partial \xi} \\ \frac{\partial N_1}{\partial \eta} & \frac{\partial N_2}{\partial \eta} & \frac{\partial N_3}{\partial \eta} & \frac{\partial N_4}{\partial \eta} \end{bmatrix} \tag{A.11}$$

while for 3-dimensional 8-node linear "brick" elements we have:

$$\underset{3\times1}{\{\nabla p\}} = \begin{Bmatrix} \frac{\partial p}{\partial x} \\ \frac{\partial p}{\partial y} \\ \frac{\partial p}{\partial z} \end{Bmatrix}, \quad \underset{8\times1}{\{p^N\}} = \begin{Bmatrix} p^1 \\ p^2 \\ p^3 \\ \vdots \\ p^7 \\ p^8 \end{Bmatrix}, \quad \underset{3\times8}{[B]} = \underset{3\times3}{[J]^{-1}} \underset{3\times8}{[N']}, \quad \underset{3\times8}{[N']} = \begin{bmatrix} \frac{\partial N_1}{\partial \xi} & \frac{\partial N_2}{\partial \xi} & \cdots & \frac{\partial N_7}{\partial \xi} & \frac{\partial N_8}{\partial \xi} \\ \frac{\partial N_1}{\partial \eta} & \frac{\partial N_2}{\partial \eta} & \cdots & \frac{\partial N_7}{\partial \eta} & \frac{\partial N_8}{\partial \eta} \\ \frac{\partial N_1}{\partial \zeta} & \frac{\partial N_2}{\partial \zeta} & \cdots & \frac{\partial N_7}{\partial \zeta} & \frac{\partial N_8}{\partial \zeta} \end{bmatrix} \tag{A.12}$$

Appendix B

Consistent Moduli

In this section we derive the so called "consistent moduli" needed in the implementation in a finite element setting. We note that:

$$d\boldsymbol{\sigma}^e = 2Gd\mathbf{e} \tag{B.1}$$

$$d\sigma_e^e = 2G\mathbf{N} : d\boldsymbol{\varepsilon} = 2G\mathbf{N} : d\mathbf{e}, \text{ and} \tag{B.2}$$

$$d\mathbf{N} = \frac{2G}{\sigma_e^e}\left(\frac{3}{2}\boldsymbol{\mathcal{K}} - \mathbf{NN}\right) : d\boldsymbol{\varepsilon} = \frac{2G}{\sigma_e^e}\left(\frac{3}{2}\boldsymbol{\mathcal{K}} - \mathbf{NN}\right) : d\mathbf{e} \tag{B.3}$$

Using (2.23) one has

$$\begin{aligned} &d\sigma_e^e - 3Gd\Delta\bar{\varepsilon}^p - \frac{\partial\sigma_y}{\partial\bar{\varepsilon}^p}d\Delta\bar{\varepsilon}^p - \frac{\partial\sigma_y}{\partial C_L}dC_L = 0 \;\Rightarrow \\ &d\Delta\bar{\varepsilon}^p = \frac{2G}{L}\mathbf{N} : d\boldsymbol{\varepsilon} - \frac{h_c}{L}dC_L \equiv \frac{\partial\bar{\varepsilon}^p}{\partial\boldsymbol{\varepsilon}} : d\boldsymbol{\varepsilon} + \frac{\partial\bar{\varepsilon}^p}{\partial C_L}dC_L, \quad L = 3G + h \end{aligned} \tag{B.4}$$

Also, from (2.20) we have

$$\begin{aligned} &d\mathbf{s}_{n+1} = d\mathbf{s}^e - 2G\left(d\Delta\bar{\varepsilon}^p\mathbf{N}_{n+1} + \Delta\bar{\varepsilon}^p d\mathbf{N}_{n+1}\right) \;\Rightarrow \\ &d\mathbf{s}_{n+1} = 2Gd\mathbf{e} - 2G\left[\left(\frac{2G}{L}\mathbf{N} : d\boldsymbol{\varepsilon} - \frac{h_c}{L}dC_L\right)\mathbf{N} + \Delta\bar{\varepsilon}^p\frac{2G}{\sigma_e^e}\left(\frac{3}{2}\boldsymbol{\mathcal{K}} - \mathbf{NN}\right) : d\boldsymbol{\varepsilon}\right] \Rightarrow \\ &d\mathbf{s}_{n+1} = 2G\boldsymbol{\mathcal{K}} : d\mathbf{e} - 2G\mathbf{N}\left(\frac{2G}{L}\mathbf{N} : d\boldsymbol{\varepsilon} - \frac{h_c}{L}dC_L\right) - \frac{4G^2\Delta\bar{\varepsilon}^p}{\sigma_e^e}\left(\frac{3}{2}\boldsymbol{\mathcal{K}} - \mathbf{NN}\right) : d\boldsymbol{\varepsilon} \;\Rightarrow \\ &d\mathbf{s}_{n+1} = 2G\boldsymbol{\mathcal{K}} : d\boldsymbol{\varepsilon} - 2G\mathbf{N}\left(\frac{2G}{L}\mathbf{N} : d\boldsymbol{\varepsilon} - \frac{h_c}{L}dC_L\right) - \frac{4G^2\Delta\bar{\varepsilon}^p}{\sigma_e^e}\left(\frac{3}{2}\boldsymbol{\mathcal{K}} - \mathbf{NN}\right) : d\boldsymbol{\varepsilon} \;\Rightarrow \\ &d\mathbf{s} = \left\{2G\boldsymbol{\mathcal{K}} - 4G^2\left[\frac{1}{L}\mathbf{NN} + \frac{\Delta\bar{\varepsilon}^p}{\sigma_e^e}\left(\frac{3}{2}\boldsymbol{\mathcal{K}} - \mathbf{NN}\right)\right]\right\} : d\boldsymbol{\varepsilon} + 2G\frac{h_C}{L}\mathbf{N}dC_L \end{aligned} \tag{B.5}$$

Equation (2.18) also implies that

$$
\begin{aligned}
dp &= \kappa\left(d\boldsymbol{\varepsilon}_{kk} - \frac{\partial \boldsymbol{\varepsilon}^h_{kk}}{\partial c}dc\right) = \kappa\left[d\boldsymbol{\varepsilon}_{kk} - frac\partial\boldsymbol{\varepsilon}^h_{kk}\partial c\left(\frac{\partial c}{\partial \bar{\varepsilon}^p}d\bar{\boldsymbol{\varepsilon}}^p + \frac{\partial c}{\partial C_L}\right)\right] \;\Rightarrow \\
dp &= \kappa\left\{\boldsymbol{\delta} : d\boldsymbol{\varepsilon} - \frac{\partial \boldsymbol{\varepsilon}^h_{kk}}{\partial c}\left[\frac{\partial c}{\partial \bar{ve}^p}\left(\frac{2G}{L}\mathbf{N} : d\boldsymbol{\varepsilon} - \frac{h_C}{L}dC_L\right) + \frac{\partial c}{\partial C_L}dC_L\right]\right\} \;\Rightarrow \\
dp &= \left\{\kappa\boldsymbol{\delta} : d\boldsymbol{\varepsilon} - \frac{\partial \boldsymbol{\varepsilon}^h_{kk}}{\partial c}\frac{\partial c}{\partial \bar{\varepsilon}^p}\left(\frac{2G}{L}\mathbf{N} : d\boldsymbol{\varepsilon} - \frac{h_C}{L}dC_L\right) - \frac{\partial \boldsymbol{\varepsilon}^h_{kk}}{\partial c}\frac{\partial c}{\partial C_L}dC_L\right\} \;\Rightarrow \\
dp &= \left\{\kappa\boldsymbol{\delta} : d\boldsymbol{\varepsilon} - \frac{\partial \boldsymbol{\varepsilon}^h_{kk}}{\partial c}\frac{\partial c}{\partial \bar{\varepsilon}^p}\frac{2G}{L}\mathbf{N} : d\boldsymbol{\varepsilon} + \frac{\partial \boldsymbol{\varepsilon}^h_{kk}}{\partial c}\frac{\partial c}{\partial \bar{\varepsilon}^p}\frac{h_C}{L}dC_L - \frac{\partial \boldsymbol{\varepsilon}^h_{kk}}{\partial c}\frac{\partial c}{\partial C_L}dC_L\right\} \;\Rightarrow \\
dp &= \kappa\left(\boldsymbol{\delta} - \frac{2G}{L}\frac{\partial \boldsymbol{\varepsilon}^h_{kk}}{\partial c}\frac{\partial c}{\partial \bar{\varepsilon}^p}\mathbf{N}\right) : d\boldsymbol{\varepsilon} + \kappa\frac{\partial \boldsymbol{\varepsilon}^h_{kk}}{\partial c}\left(\frac{h_C}{L}\frac{\partial c}{\partial \bar{\varepsilon}^p} - \frac{\partial c}{\partial C_L}\right)dC_L
\end{aligned}
\tag{B.6}
$$

Finally,

$$
\begin{aligned}
d\boldsymbol{\sigma} =& d\mathbf{s} + dp\boldsymbol{\delta} \;\Rightarrow \\
d\boldsymbol{\sigma} =& \left\{2G\boldsymbol{\mathcal{K}} - 4G^2\left[\frac{1}{L}\mathbf{NN} + \frac{\Delta\bar{\varepsilon}^p}{\sigma^e_e}\left(\frac{3}{2}\boldsymbol{\mathcal{K}} - \mathbf{NN}\right)\right] + \kappa\boldsymbol{\delta}\boldsymbol{\delta} - \kappa\frac{2G}{L}\frac{\partial \boldsymbol{\varepsilon}^h_{kk}}{\partial c}\frac{\partial c}{\partial \bar{\varepsilon}^p}\boldsymbol{\delta}\mathbf{N}\right\} : d\boldsymbol{\varepsilon} + \\
& \left[2G\frac{h_C}{L}\mathbf{N} + \kappa\frac{\partial \boldsymbol{\varepsilon}^h_{kk}}{\partial c}\left(\frac{\partial h_C}{L}\frac{\partial c}{\partial \bar{\varepsilon}^p} - \frac{\partial c}{\partial C_L}\right)\boldsymbol{\delta}\right]dC_L \;\Rightarrow \\
d\boldsymbol{\sigma} =& \left\{\boldsymbol{\mathcal{C}}^e - 4G^2\left[\frac{1}{L}\mathbf{NN} + \frac{\Delta\bar{\varepsilon}^p}{\sigma^e_e}\left(\frac{3}{2}\boldsymbol{\mathcal{K}} - \mathbf{NN}\right)\right] - \kappa\frac{2G}{L}\frac{\partial \boldsymbol{\varepsilon}^h_{kk}}{\partial c}\frac{\partial c}{\partial \bar{\varepsilon}^p}\boldsymbol{\delta}\mathbf{N}\right\} : d\boldsymbol{\varepsilon} + \\
& \left[2G\frac{h_C}{L}\mathbf{N} + \kappa\frac{\partial \boldsymbol{\varepsilon}^h_{kk}}{\partial c}\left(\frac{h_C}{L}\frac{\partial c}{\partial \bar{\varepsilon}^p} - \frac{\partial c}{\partial C_L}\right)\boldsymbol{\delta}\right]dC_L
\end{aligned}
\tag{B.7}
$$

Here we need $c\left(\bar{\varepsilon}^p, C_L\right)$, $\frac{\partial c}{\partial \bar{\varepsilon}^p}$, and $\frac{\partial c}{\partial C_L}$ to find $h \equiv \frac{\partial \sigma_y}{\partial \bar{\varepsilon}^p}$ and $h_c \equiv \frac{\partial \sigma_y}{\partial C_L}$. From (B.7) we arrive at:

$$
\frac{\partial \boldsymbol{\sigma}}{\partial \boldsymbol{\varepsilon}} = \boldsymbol{\mathcal{C}}^e - 4G^2\left[\frac{1}{L}\mathbf{NN} + \frac{\Delta\bar{\varepsilon}^p}{\sigma^e_e}\left(\frac{3}{2}\boldsymbol{\mathcal{K}} - \mathbf{NN}\right)\right] - \kappa\frac{2G}{L}\frac{\partial \boldsymbol{\varepsilon}^h_{kk}}{\partial c}\frac{\partial c}{\partial \bar{\varepsilon}^p}\boldsymbol{\delta}\mathbf{N} \tag{B.8}
$$

$$
\frac{\partial \boldsymbol{\sigma}}{\partial C_L} = 2G\frac{h_C}{L}\mathbf{N} + \kappa\frac{\partial \boldsymbol{\varepsilon}^h_{kk}}{\partial c}\left(\frac{h_C}{L}\frac{\partial c}{\partial \bar{\varepsilon}^p} - \frac{\partial c}{\partial C_L}\right)\boldsymbol{\delta} \tag{B.9}
$$